SFTSV NSs protein is a novel tick antiviral RNAi response suppressor

Mazigh Fares[1#], Melanie McFarlane[1#], Rhys H. Parry[2#], Rozeena Arif[1], Andrew T. Clarke[1], Wael Kamel[1], Kelsey Davies[1], Lesley Bell-Sakyi[3], Marine J. Petit[4], Esther Schnettler[5,6,7], Alfredo Castello[1], Alain Kohl[1,8] & Benjamin Brennan[1*]

[1]Medical Research Council–University of Glasgow Centre for Virus Research, Glasgow, G61 1QH, Scotland, UK.
[2]School of Chemistry and Molecular Biosciences, The University of Queensland, St. Lucia 4072, Australia.
[3]Department of Infection Biology and Microbiomes, Institute of Infection, Veterinary and Ecological Sciences, University of Liverpool, Liverpool, L3 5RF, UK.
[4]Microbes, Infection & Immunity, School of Biosciences, Faculty of Health and Medical Sciences, University of Surrey, Guildford, UK
[5]Bernhard-Nocht-Institute for Tropical Medicine, 20359 Hamburg, Germany.
[6]German Centre for Infection Research (DZIF), Partner Site Hamburg-Luebeck-Borstel-Riems, 20359 Hamburg, Germany
[7]Faculty of Mathematics, Informatics and Natural Sciences, University Hamburg, 20148 Hamburg, Germany
[8]Liverpool School of Tropical Medicine, Centre for Neglected Tropical Diseases, Departments of Tropical Disease Biology and Vector Biology, Liverpool, L3 5QA, UK.

[#], joint first authors
*, Correspondence: ben.brennan@glasgow.ac.uk

ORCID:

Mazigh Fares	0000-0002-6003-9244
Melanie McFarlane	0000-0002-8392-2291
Rhys H. Parry	0000-0001-9238-1952
Rozeena Arif	0009-0007-0492-6352
Andrew T. Clarke	0000-0001-7271-3833
Wael Kamel	0000-0002-7625-2648
Kelsey Davies	0009-0009-5624-5983
Lesley Bell-Sakyi	0000-0002-7305-0477
Marine Petit	0000-0001-7427-7203
Esther Schnettler	0000-0001-8141-3728
Alfredo Castello	0000-0002-1499-4662
Alain Kohl	0000-0002-1523-9458
Benjamin Brennan	0000-0003-4707-726X

Keywords:

Bunyavirus, severe fever with thrombocytopenia syndrome virus, tick cell line, arthropod innate immune evasion, protein function, RNA-binding protein, protein-RNA interaction, RNA, host-virus interactions

Abstract

Severe fever with thrombocytopenia syndrome virus (SFTSV) is an emerging tick-borne phenuivirus causing high mortality in humans. While the non-structural protein NSs is dispensable for replication in mammalian cells, we demonstrate for the first time that NSs is essential for viral replication in tick cells. SFTSV infection triggers canonical Dicer-2-mediated antiviral RNA interference (RNAi) in tick cells, producing virus-derived small interfering RNAs (siRNAs) that target viral transcripts for degradation. We show that NSs functions as a viral suppressor of RNAi by selectively sequestering single-stranded RNAs derived from 22-nucleotide siRNAs, preventing their incorporation into RNA-induced silencing complexes (RISC). Complementation with a heterologous RNAi suppressor (p19 protein) partially rescues replication of NSs-deficient virus, validating NSs' RNAi suppressive function. These findings reveal that successful tick-borne viral replication requires host-specific immune evasion strategies and establish NSs-mediated RNAi suppression as essential for SFTSV persistence in arthropod vectors.

MAIN

Severe fever with thrombocytopenia syndrome virus (SFTSV; *Bandavirus dabieense*; *Phenuiviridae*) emerged as a significant threat to human health following its discovery in central China in 2009[1], where it was identified as the causative agent of a severe haemorrhagic fever syndrome. This tick-borne phenuivirus rapidly gained attention due to its high case fatality rate of 6-30%. Its distinctive clinical presentation is characterized by fever, thrombocytopenia, leukocytopenia, and gastrointestinal manifestations[2]. The geographic range of SFTSV has since expanded across East Asia, with confirmed cases reported in South Korea, Japan, Taiwan, and Vietnam, establishing it as a regional public health concern of growing importance[3]. Currently, no effective antiviral drugs or vaccines exist to treat SFTS disease.

SFTSV transmission occurs primarily through the bite of infected ixodid ticks, with several species identified as potential vectors[4]. *Haemaphysalis longicornis* serves as the principal vector across much of the SFTSV geographical range, while *Haemaphysalis flava* and *Rhipicephalus microplus* may also contribute to transmission cycles in specific regions[5]. Ticks acquire SFTSV through blood feeding on infected vertebrate hosts and can subsequently transmit the virus to humans and other susceptible animals. This complex ecology involves multiple tick species and some amplifying vertebrate hosts (hedgehogs and small rodents), creating diverse transmission pathways that complicate control efforts[6].

Arthropod vectors, including ticks, have evolved sophisticated innate immune mechanisms to combat viral infections, with RNA interference (RNAi) representing a primary antiviral defence pathway[7,8]. Unlike mammals, in which type I interferon responses dominate antiviral immunity[9], arthropods rely heavily on RNA silencing machinery to recognise and degrade viral nucleic acids. Tick antiviral RNAi responses produce characteristic 22-nucleotide small interfering RNAs (siRNA) through Dicer-2 processing of viral double-stranded RNA intermediates, which are subsequently incorporated into RNA-induced silencing complexes (RISC) to target complementary viral transcripts for degradation[8,10]. Distinguishing authentic virus-derived siRNAs from RNA degradation products requires methylation-sensitive approaches, as functional siRNAs undergo Hua Enhancer-1 (HEN1)-mediated 2'-O-methylation upon RISC loading[11-15]. The effectiveness of arthropod RNA silencing as an antiviral mechanism

has been demonstrated across diverse vector species (flies and mosquitoes)[16], yet our understanding of how tick-borne viruses evade or suppress these responses remains limited[17].

The evolutionary arms race between viruses and RNAi defenses has driven many viruses to evolve suppressors of RNAi (VSRs) that counteract antiviral silencing[18,19]. They employ diverse mechanisms to inhibit RNAi activity, including sequestration of siRNAs, interference with Dicer processing, and disruption of RISC assembly and function. While NSs proteins from plant-infecting tospoviruses are well-characterized RNAi suppressors that bind double-stranded siRNAs[20], vertebrate-infecting bunyaviruses show variable suppressor activities[21]. Crucially, no arthropod-specific RNAi suppression mechanisms have been definitively established for tick-borne phenuiviruses.

Despite SFTSV's emergence as a significant public health threat and evidence of vsiRNA production in infected ticks[22], the specific mechanisms by which tick-borne phenuiviruses evade or suppress arthropod RNAi responses remain unknown. While the non-structural protein (NSs) of SFTSV has been suggested as a possible RNAi suppressor[22,23], its actual role and mechanism of action in arthropod cells have yet to be definitively established.

Here, we demonstrate for the first time that SFTSV exhibits fundamentally different replication requirements in tick versus mammalian cell cultures, with NSs proving essential for viral maintenance in tick cells. Using comprehensive molecular analyses including methylation-sensitive small RNA sequencing, structural modeling, and complementation studies with heterologous suppressors, we reveal that NSs functions as a unique viral suppressor of RNAi by selectively sequestering the pool of virus-derived single stranded siRNAs away from the RNAi machinery, thereby enabling productive infection in tick cells and enhancing vector-borne transmission potential.

RESULTS

SFTSV infects cell lines derived from tick species reported to act as competent vectors.

To identify suitable tick cellular models for SFTSV infection, we tested multiple cell lines representing both *Metastriata* (*Rhipicephalus* and *Hyalomma* spp.) and *Prostriata* (*Ixodes* and *Amblyomma* spp.) lineages of the family *Ixodidae*, using wildtype (wt) SFTSV strain HB29[1,24]. Ten-day viral yield assays revealed SFTSV efficiently replicated in cell lines derived from *Rhipicephalus* and *Hyalomma* spp, evidenced by increased viral titres and nucleocapsid protein detection in infected lysates (Fig. 1A,B). SFTSV replication was minimal in phylogenetically distinct *Ixodes* and *Amblyomma* spp. tick cell lines, despite these species vectoring other members of the *Phenuiviridae* such as Uukuniemi[25] and Heartland viruses[26,27]. Given that bunyaviruses establish non-pathogenic, continuous viral production in tick cells[25,28], we monitored infectious virus production daily over 10-days at low MOI (Fig. 1C). Viral titres steadily decreased over time in *Ixodes* spp. cell lines, but continuous production was evident in *Rhipicephalus* spp. cultures. After 10 days post-infection (dpi), all cultures were split 1:2 and monitored for 14 days; clear SFTSV persistence in BME/CTVM6 and BME/CTVM23 lines (Fig. 1D) confirms their utility as robust models for studying SFTSV arthropod cell infection[29]. These results suggest SFTSV entry and replication

146 may depend on host cellular factors that vary among tick species and demonstrate
147 that permissive cell lines can maintain viable virus over extended culture periods.
148

149 **SFTSV NSs protein expression is repressed in tick cells yet is essential for**
150 **sustained virus replication.**

151 We previously established that SFTSV NSs is a potent interferon antagonist[30] and
152 virulence factor in animal models[31-33], yet dispensable for replication in mammalian
153 cell systems[34]. However, the molecular basis for NSs function in tick cells, the natural
154 arthropod vector, has remained unexplored. To address this knowledge gap, we
155 investigated NSs function during SFTSV infection of tick cells. We infected
156 BME/CTVM6 cells, selected for their robust and sustained wt SFTSV replication (Fig.
157 1A-D), with either wt or NSs-deleted (delNSs) SFTSV across a range of multiplicities
158 of infection. We observed that wt SFTSV demonstrated stable and abundant
159 production of infectious virus throughout the experiment, with SFTSV titres increasing
160 by approximately 3-$\log_{10}$ ffu/ml over the time course (Fig. 1E). In contrast, delNSs
161 SFTSV failed to maintain infectious progeny, with viral titres declining progressively
162 over the infection time course (Fig. 1F). Consistent with this, Western blot analysis of
163 delNSs SFTSV-infected cell lysates revealed no detectable nucleocapsid protein,
164 indicating complete failure to establish a productive infection in tick cells (Fig. 1G).
165 Notably, NSs protein was undetectable in cells infected with both wt and delNSs
166 SFTSV, despite this protein being detected in mammalian cell controls (Vero E6). This
167 observation was unexpected given the apparent requirement for NSs in tick cells. To
168 investigate this paradox further, we performed immunofluorescence microscopy on
169 infected BME/CTVM6 cells (Fig. 1H). Quantitative analysis revealed that delNSs
170 SFTSV infection led to only 2-8% nucleocapsid-positive cells (Fig. 1I,J). In contrast,
171 60-80% of cells were positive for nucleocapsid protein following wt SFTSV infection
172 across all tested MOIs, demonstrating efficient viral replication (Fig. 1K,L).
173

174 To gain a deeper understanding of the viral protein abundance in SFTSV infected tick
175 cells we performed proteomic analysis of BME/CTVM6 cells infected with wild-type
176 SFTSV at 3- and 6-dpi, examining both the distribution of peptide intensities (Fig. 1M)
177 and mean peptide intensities (Fig. 1N) for viral proteins NSs, nucleocapsid protein (N),
178 glycoprotein precursor (GPC), and RNA-dependent RNA polymerase (RdRp). The
179 peptide intensity distributions for NSs remained unchanged between time points, while
180 N showed a non-significant increase (P = 0.709). This reflects that N protein peptides
181 already exhibited high intensities and broad distribution at 3 dpi, suggesting a
182 detection plateau had been reached. In contrast, GPC and RdRp exhibited significant
183 increases (P = 0.026 and P = 6.23 x 10^{-12}, respectively), indicative of enhanced viral
184 replication and assembly processes (Fig. 1M). Analysis of mean peptide intensities
185 revealed temporal increases for N, GPC, and RdRp from 3 to 6 dpi, while NSs
186 maintained the lowest expression levels with minimal temporal change (Fig. 1N).
187 Notably, while NSs-derived peptides were detectable by mass spectrometry, NSs
188 protein intensity levels remained below the detection threshold of Western blot
189 analysis (Fig. 1G), suggesting tightly regulated, low-level expression of this protein.
190 This differential sensitivity between proteomic and immunoblot detection methods
191 reveals that NSs is present but maintained at substantially lower levels compared to
192 structural and replication proteins during SFTSV infection of tick cells.
193

NSs subgenomic mRNA expression is reduced in SFTSV-infected tick cells compared to mammalian cells.

The SFTSV NSs protein is encoded within the viral S segment, which employs an ambisense coding strategy to produce both NSs and the N protein, consistent with all phenuiviruses[35]. The NSs open reading frame is translated from a subgenomic mRNA transcribed from the antigenomic S RNA template following viral genome replication. To investigate the molecular basis for NSs repression in tick cells, we analysed viral RNA species derived from the S segment during infection of two *Rhipicephalus* spp. tick cell lines and compared these results to mammalian Vero E6 cells as controls.
We employed Northern blot analysis using strand-specific RNA probes to target either the N or NSs coding regions and to distinguish genomic from antigenomic RNA species (Fig. 1O). Productive viral replication was confirmed in wild-type SFTSV-infected tick cells through detection of both genomic [detected by N(-) and NSs(+) probes] and antigenomic [detected by N(+) and NSs(-) probes] S segment RNA at 6 dpi. While N mRNA was readily detectable in both tick cell lines and in the mammalian cell controls, NSs subgenomic mRNA levels were markedly reduced in tick cells compared to Vero E6 cells when probed with the NSs(+) specific probe (Fig. 1P).
The observed reduction in NSs subgenomic mRNA levels in tick cells provides a plausible explanation for the diminished NSs protein expression during infection. However, the underlying mechanism, whether due to transcriptional attenuation or altered RNA stability, remains unresolved. While our Northern blot data confirm reduced mRNA accumulation, further investigation is needed to determine whether this reflects regulated transcription termination, selective degradation or post-transcriptional silencing. This finding also raises important questions about how NSs functions during early infection, before its apparent repression.

SFTSV infection triggers small RNA production in tick cells.

Given that tick cells rely on RNAi as a primary antiviral defence mechanism, we next examined whether wt SFTSV replication, and specifically NSs mRNA, is targeted by the tick RNAi pathway. To determine whether the observed reduction in SFTSV NSs mRNA reflected targeted RNAi-mediated degradation, we used beta elimination to distinguish between RISC-loaded siRNAs, unloaded siRNAs, and RNA degradation products. Small RNA samples were therefore subjected to beta elimination prior to sequencing analysis. This treatment selectively removes degradation fragments and non-methylated siRNAs containing 2',3'-cyclic phosphate termini while preserving HEN1-methylated, RISC-loaded siRNAs bearing 5'-phosphate and 3'-hydroxyl groups[11-15]. Since both degradation products and non-RISC-loaded siRNAs exhibit similar size distributions (20-24 nt), protection by HEN1 methylation during beta elimination enables unambiguous identification of functional vsiRNAs and confirms RNAi pathway activation against SFTSV[12,13].
The efficacy of beta elimination was validated in uninfected BME/CTVM6 cells or *Aedes aegypti* AF525 cells, an Ago2-deficient *Aedes aegypti* cell line, (Supplementary Fig. 1) and Semliki Forest virus (SFV)-infected AF525 cells (Supplementary Fig. 2A,B) by published methodologies[11]. Following SFTSV infection of BME/CTVM6 cells, approximately 10^5 reads within the small RNA size range (18-30 nt) mapped to each SFTSV genomic segment in untreated samples, with read abundance increasing between 3- and 6-dpi. Although beta elimination reduced overall read counts, the proportional increase in reads mapping to SFTSV RNAs from 3 to 6 dpi was preserved,

242 indicating sustained small RNA responses targeting SFTSV throughout infection (Fig.
243 2A).
244 The 5' nucleotide composition of all 22 nt vsiRNAs showed strong bias toward uridine
245 and adenine residues, consistent with arthropod Dicer-2 processing specificity[36]. Beta
246 elimination treatment virtually eliminated the 22 nt peak at both time points, indicating
247 these vsiRNAs lacked 3'-terminal methylation and remained susceptible to chemical
248 modification (Fig. 2B,C). Analysis of vsiRNAs mapping to SFTSV genome and
249 antigenome sequences at both 3- and 6-dpi revealed pronounced enrichment for 22
250 nt species in untreated samples, with comparable distributions observed for genomic
251 and antigenomic reads (Fig. 2D,E). Conversely, longer small RNAs (24-30 nt) were
252 largely unaffected by beta elimination, consistent with 2'-O-methylated piRNAs or
253 degradation fragments that escaped chemical treatment.
254 Notably, the selective loss of Dicer-2-processed 22 nt reads following beta elimination
255 at 3 dpi demonstrates that the majority of SFTSV-derived siRNAs in BME/CTVM6 cells
256 lack methylation modifications, suggesting exclusion from functional Ago2-containing
257 RISC complexes (Fig. 2D). However, this transient suppression of vsiRNAs from Ago2
258 is eventually overwhelmed by 6 dpi, evidenced by the strong 22 nt peak of methylated-
259 vsiRNAs in the beta-eliminated sample, indicating a resumption in the targeting of viral
260 RNA sequences by the RNAi machinery (Fig. 2E).
261 While HEN1-mediated methylation of RISC-loaded siRNAs is conserved from plants
262 to arthropods[12,37], the dynamics of this process during viral infection in tick cells have
263 not been previously characterized. Our detection of methylated small RNAs in mock-
264 infected controls (Supplementary Fig. 1) and their recovery at 6 dpi confirms that
265 BME/CTVM6 cells possess functional HEN1 methylation machinery. Therefore, the
266 selective absence of methylated SFTSV-specific siRNAs at 3 dpi (Fig. 2D), followed
267 by their subsequent accumulation at 6 dpi (Fig. 2E), indicates active viral suppression
268 of RNAi responses during early infection that is eventually overcome by sustained
269 antiviral pressure, enabling initial viral replication. The observed NSs transcript
270 degradation supports this interpretation (Fig. 1P), demonstrating that functional RNAi
271 activity ultimately prevails despite initial viral evasion mechanisms.
272

273 **RNAi-mediated vsiRNA targeting exhibits temporal dynamics and segment-**
274 **specific preferences across the SFTSV genome.**

275 Given that 22-nt species constituted the predominant small RNA population (which
276 corresponds to the typical length of vsiRNAs produced in tick cells), we mapped
277 vsiRNA coverage across genomic and antigenomic strands of the SFTSV small (S;
278 Fig. 2F), medium (M; Fig. 2G), and large (L; Fig. 2H) segments at 3- and 6-dpi in
279 untreated and beta-eliminated samples. SFV served as a control for beta-elimination
280 efficacy and mapping specificity (Supplementary Fig. 2C,D).
281 SFTSV vsiRNA accumulation increased substantially between 3- and 6-dpi across all
282 segments, indicating progressive amplification of the RNAi response. In untreated
283 samples, the M and L segments exhibited extensive targeting, with pronounced
284 accumulation at untranslated regions and segment termini. Beta-elimination confirmed
285 sustained SFTSV targeting by the tick RNAi machinery, demonstrating that observed
286 signals represent authentic vsiRNAs rather than 2'-O-methylated small RNA
287 contaminants. Notably, the S segment displayed concentrated targeting within the
288 intergenic region and the NSs open reading frame on the genomic strand, particularly
289 around the areas previously identified as the transcription termination sites for the N
290 and NSs mRNAs[34], indicating RNAi-mediated cleavage of both genomic RNA and NSs

291 subgenomic transcripts. This finding provides a mechanistic explanation for the
292 reduced NSs mRNA detection observed by Northern blot analysis (Fig. 1P). The
293 strand-specific and segment-preferential targeting patterns demonstrate that tick cells
294 mount a sophisticated, temporally regulated antiviral RNAi response against SFTSV
295 infection, which the wt virus can overcome, yet a NSs-deletant virus cannot.
296

297 **SFTSV infection triggers canonical Dicer-2-mediated vsiRNA production in tick**
298 **cells.**

299 To characterise the dsRNA cleavage patterns during SFTSV infection, we analysed
300 small RNA overlap profiles and strand complementarity patterns mapping to viral
301 segments at 3- and 6-dpi (Fig. 3). At both timepoints, viral small RNAs predominantly
302 exhibited 20-22 nucleotide lengths with a clear preference for 20 nucleotide overlaps
303 between complementary strands (Fig. 3A,C). Strand overlap analysis revealed
304 enhanced complementarity at positions resulting in 2 nucleotide 3' overhangs,
305 characteristic of canonical Dicer-2 cleavage products (Fig. 3B,D). The average z-score
306 across all three genome segments increased from 1.98 at 3 dpi to 2.54 at 6 dpi,
307 suggesting sustained Dicer-2 activity throughout viral replication. Notably, virus-
308 derived small RNAs in the 20-24 nucleotide range all displayed this complementarity
309 pattern across the L, M, and S viral segments, indicating uniform processing.
310 No evidence of antiviral vpiRNAs (viral PIWI-interacting RNAs) was detected in the
311 expected 24-30 nt range in infected tick cells at either timepoint. As a methodological
312 control, SFV-infected AF525 cells displayed the characteristic sharp 19 nucleotide
313 overlap signature resulting from impaired passenger strand processing in the absence
314 of functional Ago2, along with piRNA signatures in the 24-30 nucleotide range with 10
315 nucleotide overlaps, as previously documented[11] (Supplementary Fig. 3). This
316 contrasts with the broader overlap patterns observed in tick cells, confirming the host
317 species-specific nature of antiviral RNA processing mechanisms.
318

319 **Viral RNA silencing suppressor partially rescues replication-defective SFTSV in**
320 **tick cells.**

321 The findings above suggested SFTSV NSs functions as an RNA silencing suppressor
322 in tick cells. To test this hypothesis, we engineered a recombinant delNSs SFTSV
323 expressing the tomato bushy stunt virus (TBSV) p19 protein, a well-characterized RNA
324 silencing suppressor that sequesters siRNAs to counteract antiviral RNA
325 interference[38,39]. Both delNSs-p19V5 and delNSs-eGFP control viruses replicated
326 efficiently in mammalian Vero cells, confirming viral viability and demonstrating again
327 that NSs is dispensable for replication in mammalian systems (Supplementary Fig.
328 4A,B). In contrast, these viruses showed markedly different phenotypes in tick cells.
329 Wild-type SFTSV established robust infection with abundant viral N protein foci in
330 BME/CTVM6 cells (Fig. 4A), while delNSs-eGFP showed no detectable infection by
331 immunofluorescence (Fig. 4B) and no viral proteins by Western blot (Fig. 4C).
332 Critically, functional complementation with p19 partially rescued the replication-
333 defective phenotype, enabling viral persistence and limited local spread as evidenced
334 by discrete N protein foci at 6 dpi (Fig. 4D,E). Western blot analysis confirmed viral N
335 protein expression and V5-tagged p19 detection in delNSs-p19V5 infected cells (Fig.
336 4C). Growth kinetics revealed that delNSs-p19V5 achieved only intermediate
337 replication levels with declining viral titers over time, indicating that viral replication can
338 be recovered in tick cells (Fig. 4F). These complementation studies support a role for

339 NSs in counteracting tick antiviral responses. To elucidate the underlying mechanism,
340 we next investigated the biochemical properties of NSs.
341

342 **SFTSV NSs exhibits structural features consistent with RNA-binding activity.**

343 Given that RNA silencing suppression typically requires direct interaction with RNA
344 substrates, we investigated whether NSs functions as an RNA-binding protein. We
345 generated a high-confidence structural model of the NSs protein using AlphaFold2[40,41]
346 (Fig. 5A and Supplementary Fig. 5). The predicted structure revealed a compact
347 globular protein with multiple α-helical regions and β-sheet domains. Electrostatic
348 surface analysis demonstrated several distinct positively charged patches distributed
349 across the protein surface (Fig. 5B), a characteristic feature of nucleic acid-binding
350 proteins that facilitates interaction with the negatively charged phosphate backbone of
351 RNA. We next employed computational approaches to identify potential RNA-binding
352 domains (RBDs) within the NSs sequence. RBDetect analysis, which identifies RNA-
353 binding sites based on sequence homology to known cellular RNA-binding
354 sequences[42,43], revealed two discrete regions with significant similarity to established
355 RBDs: residues SER13-ARG22 and TRP133-THR141 (Fig. 5C; Supplementary Table
356 1). The probability scores for RNA-binding activity peaked at approximately 0.9 for the
357 first region and 0.6 for the second region, indicating strong predicted binding potential.
358 To validate these predictions using an independent approach, we applied BindUP
359 analysis, which predicts RNA-binding sites based on surface physicochemical
360 properties[44] (Supplementary Table 2). This analysis identified a region within α-helix 9
361 as having high probability for nucleic acid interaction. Notably, when the outputs from
362 both RBDetect and BindUP were mapped onto the AlphaFold2 structural model, the
363 predicted binding sites showed substantial overlap with spatial continuity (Fig. 5D),
364 strengthening confidence in these predictions. Importantly, all identified putative RBDs
365 were located within regions of high structural confidence in the AlphaFold2 model
366 (Supplementary Fig. 5E).
367

368 **SFTSV NSs binds 22 nt vsiRNAs in infected cells.**

369 To validate NSs as an RNA-binding protein, we performed immunoprecipitation of V5-
370 tagged p19 and NSs from recombinant virus-infected BME/CTVM6 cells at 2 dpi.
371 Although protein expression levels in whole cell lysates varied between replicates,
372 both proteins were detected in immunoprecipitated samples (Fig. 6A). Small RNA-seq
373 analysis of co-immunoprecipitated RNAs revealed that p19 lysates were enriched for
374 19-22 nt RNAs as expected[45], whereas NSs immunoprecipitates showed enrichment
375 for 22 nt RNAs (the characteristic products of Dicer-2 processing) which comprised
376 50-55% of all detected reads across three independent replicates (Fig. 6B).
377 Analysis of small RNA composition demonstrated that 22 nt reads accounted for 75%
378 of mapped reads derived primarily from SFTSV RNA in NSs immunoprecipitates, with
379 approximately 45% from antigenomic sense and 30% from genomic sense sequences.
380 In contrast, p19-associated SFTSV siRNAs were approximately 20nt in length, though
381 this varied between replicates (Fig. 6C; Supplementary Fig. 6). When comparing
382 normalized read counts across viral genome segments, both proteins showed similar
383 binding levels, although siRNAs derived from the SFTSV M segment were the most
384 reproducibly immunoprecipitated by NSs across replicates (Fig. 6D).
385 Genome mapping analysis revealed distinct siRNA mapping patterns between the two
386 proteins. The p19-associated 22 nt siRNAs mapped to limited viral genome regions

387 (Fig. 6E, Supplementary Fig. 7), whereas NSs-bound 22 nt RNAs mapped to multiple
388 reproducible hotspots distributed across all three viral segments (Fig. 6F,
389 Supplementary Fig. 8). Notably, hotspots derived from antigenomic sense S segment
390 RNA corresponded to regions within the genome with strongly predicted secondary
391 structures, such as the siRNA hotspot identified mapping to nt position 1210-1238 of
392 the antigenomic S RNA, which corresponds to the head region of a hairpin structure
393 (Fig. 6F; Supplementary Fig. 9).
394 Crucially, NSs immunoprecipitation revealed a statistically significant reduction (**$p \leq$
395 0.01) in the proportion of 22 nt siRNA duplex pairs (those with 20 nt overlaps),
396 decreasing from approximately 45% in total infected cell lysates to less than 10% in
397 NSs-bound samples. This reduction was specific to vsiRNAs, as *R. microplus*
398 genome-derived siRNAs showed no difference in duplex abundance (Fig. 6G). Size-
399 specificity analysis confirmed similar single-strand enrichment for 21 nt and 23 nt
400 siRNAs but not for 24 nt or 28 nt species, demonstrating that NSs selectively binds
401 vsiRNA single strands within a defined size range (Supplementary Fig. 10). This
402 sequestration likely occurs post-Dicer processing, as correctly processed vsiRNA
403 duplexes were robustly and reproducibly detected in infected tick cells (Fig. 3). These
404 findings support a model in which NSs suppresses RNAi by selectively sequestering
405 single-stranded 22-nt vsiRNAs, likely at a step preceding their incorporation into RISC.
406 The observed reduction in duplex vsiRNA abundance, combined with structural
407 predictions, provides strong support for this mechanism. However, direct evidence of
408 impaired Argonaute loading, such as through Ago2 immunoprecipitation or silencing
409 reporter assays, has yet to be demonstrated. Whether NSs binding fully blocks RISC
410 assembly or transiently delays vsiRNA incorporation to permit productive viral
411 replication remains to be determined. The molecular details and stoichiometric
412 requirements of NSs–vsiRNA interactions warrant further investigation.
413
414 To validate our computational predictions, we performed molecular modelling using
415 authentic 22-nucleotide vsiRNAs identified from NSs immunoprecipitation
416 (Supplementary Table 3). Docking analyses revealed multiple RNA-binding interfaces
417 within 4Å contact distance for vsiRNAs derived from all three SFTSV genomic
418 segments: S (Fig. 6H), M (Fig. 6I), and L (Fig. 6J).
419 Notably, the predicted RNA contact residues clustered within the same protein region
420 identified by both RBdetect and BindUP algorithms (Fig. 5D), providing highly
421 convergent evidence for the location of functional RNA-binding sites from orthogonal
422 computational approaches. This structural validation strongly supports the siRNA-
423 binding capacity of SFTSV NSs protein in tick cells and establishes a molecular
424 framework for understanding NSs-mediated RNAi suppression.
425
426 **DISCUSSION**
427 This study reveals a fundamental dichotomy in SFTSV replication strategies between
428 mammalian and arthropod hosts, establishing NSs as a critical RNA silencing
429 suppressor essential for tick cell infection. The striking observation that NSs protein is
430 virtually undetectable in productively-infected tick cells, despite being absolutely
431 required for viral replication, challenges conventional paradigms of viral protein
432 function and highlights the sophisticated evolutionary adaptations that enable arboviral
433 transmission.
434 The species-specific permissivity patterns observed across tick cell lines (Fig. 1A,B)
435 provide crucial insights into possible SFTSV vector competence. The successful
436 replication in *R. microplus* cells (BME/CTVM6 and BME/CTVM23) mirrors the known

437 epidemiological distribution of SFTSV-positive ticks, suggesting that cellular factors
438 governing viral entry and replication are phylogenetically conserved traits that
439 determine vector competence in nature. Cell lines from two other species,
440 *Rhipicephalus decoloratus* (BDE/CTVM16) and *Hyalomma anatolicum* (HAE/CTVM9)
441 originating from East Africa and India respectively, also supported SFTSV replication,
442 although the virus has not been reported from these tick species or geographic
443 regions, suggesting the potential for spread beyond its currently known distribution.
444 The sustained viral production over extended culture periods (Fig. 1C,D) confirms the
445 establishment of infections expected of arthropod-borne bunyaviruses[25,28,46,47]. The
446 failure of SFTSV to replicate in *Ixodes* spp. cell lines, despite these ticks vectoring
447 related phenuiviruses[48], indicates that host range determinants may operate at the
448 cellular level.
449 Here we show that SFTSV NSs protein expression is repressed in tick cells yet is
450 unexpectedly essential for sustained virus replication. This contrasts with mosquito-
451 borne bunyaviruses such as Rift Valley fever virus, where NSs repression does not
452 impact virus replication in mosquito cells and instead facilitates viral persistence[47,49-
453 51], suggesting distinct host-specific requirements for NSs in different arthropod
454 vectors. The paradoxical requirement for NSs in tick cells represents a remarkable
455 evolutionary balancing act that extends beyond recent findings in mammalian
456 systems[23]. Our demonstration that delNSs SFTSV fails to sustain infectious progeny
457 in tick cells (Fig. 1F) and showed no detectable nucleocapsid protein (Fig. 1G),
458 contrasts sharply with dispensable NSs function in mammalian cells[34]. Proteomic
459 analysis revealed differential temporal expression of SFTSV proteins in tick cells, with
460 structural proteins (N, GPC) and the RNA-dependent RNA polymerase (RdRp)
461 showing significant increases from 3 to 6 dpi, while the non-structural protein NSs
462 remained at consistently low levels throughout infection. The detection of NSs by mass
463 spectrometry despite its absence in Western blots suggests tight regulation of this
464 protein in infected tick cells, perhaps compounded by antbody sensitivity (Fig. 1G,H).
465 The paradox of NSs essentiality despite undetectable protein levels may be resolved
466 through several non-exclusive mechanisms. Firstly, based on established proteomics
467 intensity-to-concentration relationships[52,53], the observed mean peptide intensity for
468 SFTSV NSs (Log2 = 15) suggests protein concentrations in the low nanomolar range
469 (1-10 nM) range, which, while below Western blot detection limits, align with the
470 nanomolar binding affinities characteristic of other viral RNA silencing suppressors[54].
471 Nevertheless, future direct quantification of NSs:vsiRNA binding stoichiometry, and
472 assessment of competitive Ago2 loading inhibition *in vivo*, will be essential to
473 experimentally validate this proposed depletion mechanism; Second, NSs may exhibit
474 exceptionally high RNA-binding affinity or cooperative binding that amplifies its
475 suppressive capacity at low concentrations; Third, temporal or subcellular
476 compartmentalization may concentrate NSs activity during critical early infection
477 phases, when RNAi activation would otherwise prevent productive replication. The
478 profound replication defect observed in NSs-deficient infections (Fig. 1I,J) reinforces
479 the notion that even low-abundance NSs is functionally essential in tick cells. These
480 mechanisms may collectively explain how limited quantities of NSs achieve effective
481 RNAi suppression in the tick host.
482
483 The selective reduction of NSs subgenomic mRNA in tick cells provides a mechanistic
484 explanation for the protein's low abundance while maintaining its essential function.
485 Our Northern blot analysis (Fig. 1P) demonstrates that while both genomic and
486 antigenomic viral RNAs accumulate to similar levels in tick and mammalian cells, NSs

mRNA shows markedly reduced levels specifically in tick cells, suggesting a post-transcriptional regulation mechanisms unique to arthropod hosts. This regulatory strategy represents an evolutionary compromise that maximizes NSs activity during critical early infection phases while minimizing detection by host surveillance mechanisms.

The demonstration that SFTSV infection triggers robust small RNA production in tick cells (Fig. 2A) establishes RNAi as a primary antiviral defence mechanism. Our beta elimination analyses definitively prove that the observed 22-nucleotide small RNAs represent authentic virus-derived siRNAs rather than degradation products (Fig. 2B-E). This finding significantly extends previous work by Xu *et al.*, who demonstrated vsiRNA production during SFTSV infection of *Haemaphysalis longicornis* through blood feeding[22]. Our study advances this understanding by providing detailed mechanistic insights into vsiRNA processing, demonstrating temporal dynamics of the RNAi response, and establishing the functional consequences for viral replication in cell culture systems.

The emergence of methylated vsiRNAs at 6 dpi (Fig. 2E), which are absent at 3 dpi, supports a model wherein the host RNAi machinery eventually overcomes transient viral suppression. Given that NSs is expressed at low levels in infected tick cells (undetectable by Western blot; Fig. 1G), complete sequestration of all vsiRNAs would present a significant stoichiometric challenge. This constraint is further amplified by the temporal dynamics of antiviral RNAi responses, as vsiRNA accumulation increases substantially between 3 and 6 dpi. The appearance of RISC-loaded vsiRNAs at 6 dpi therefore indicates that sustained RNAi pathway activation can ultimately saturate the suppressive capacity of this low-abundance viral suppressor, enabling functional antiviral silencing despite initial evasion mechanisms.

Our observations support a 'depletion strategy' whereby viral suppressors of RNAi achieve functional suppression without requiring abundant expression. To address potential stoichiometric limitations, we propose that NSs operates through high-affinity binding kinetics rather than simple mass action. Assuming dissociation constants comparable to characterized VSRs (Kd ~0.1-1 nM[54]) and estimated cellular vsiRNA concentrations of 10-100 nM during peak infection, even low-abundance NSs could effectively compete for substrate binding. Additionally, preferential sequestration of newly processed single-stranded guide RNAs before RISC loading would be more efficient than competing with mature RISC complexes, explaining how limited NSs quantities can achieve functional suppression despite abundant total vsiRNA pools. Such high-affinity interactions are characteristic of other viral RNAi suppressors, including tombusvirus p19, which functions at substoichiometric concentrations (Kd ~ 0.17 nM) and achieves >90% siRNA depletion despite limited protein abundance[45].

The progressive amplification of vsiRNA accumulation across all viral segments between 3- and 6-dpi (Fig. 2F-H) indicates that tick cells mount increasingly robust antiviral responses over time. The concentrated targeting within the unencapsidated S segment intergenic region[55] and NSs open reading frame provides direct mechanistic evidence for RNAi-mediated NSs mRNA degradation, explaining the reduced NSs protein levels observed. This segment-specific targeting pattern suggests that viral RNA secondary structures or transcript abundance influence RNAi machinery accessibility, with implications for understanding viral evolutionary constraints.

537 The demonstration of canonical Dicer-2-mediated vsiRNA production through strand
538 overlap analysis (Fig. 3) confirms that tick antiviral RNAi pathways follow established
539 arthropod paradigms. The predominance of 20-22 nucleotide products with
540 characteristic 2-nucleotide 3' overhangs indicates uniform processing across all viral
541 segments[8]. Notably, the absence of detectable vpiRNA responses contrasts with
542 mosquito antiviral systems[46,56-59], suggesting lineage-specific adaptations in arthropod
543 small RNA-mediated immunity. However, the complete absence of vpiRNA production
544 warrants further mechanistic investigation to determine whether this reflects genuine
545 pathway absence or differential regulation.
546
547 The successful complementation of NSs-deficient virus with the heterologous p19
548 suppressor (Fig. 4) provides strong evidence that NSs functions as an RNAi
549 suppressor in tick cells. The partially restored viral protein expression and intermediate
550 replication kinetics in delNSs-p19V5 infected cells demonstrate functional
551 complementation while revealing that NSs possesses unique properties beyond
552 simple siRNA sequestration. This incomplete complementation suggests NSs may: (i)
553 exhibit specific binding preferences for SFTSV-derived vsiRNAs through evolved
554 sequence or structural recognition motifs, (ii) interact with additional host factors
555 beyond the core RNAi machinery, or (iii) function through temporal coordination with
556 other viral proteins during the replication cycle. The heterologous p19 suppressor,
557 while functionally competent, lacks these virus-specific adaptations that have co-
558 evolved to optimise NSs performance within the SFTSV life cycle.
559
560 Our integrated structural and functional analyses establish NSs as a novel siRNA-
561 binding protein that selectively sequesters 22 nt vsiRNAs through size-specific
562 molecular recognition. This finding extends the established paradigm of bunyaviral
563 RNA silencing suppression beyond the well-characterized tospoviral NSs proteins,
564 which bind both siRNAs and miRNAs with varying specificity depending on
565 phylogenetic origin; American clade tospoviruses exhibit broad-spectrum binding to
566 both long and short dsRNA molecules, whereas Eurasian clade NSs proteins
567 demonstrate restricted binding to short dsRNA substrates[20,60,61]. Notably, while RNA
568 silencing suppressor activity has not been clearly demonstrated for NSs proteins from
569 vertebrate-infecting bunyaviruses in either vertebrate hosts or arthropod vectors[20], our
570 results provide definitive mechanistic evidence for this function. Javaid *et al*.[23] recently
571 demonstrated SFTSV NSs interacts with AGO2 to regulate RNAi in mammalian cells.
572 However, our work provides the first direct evidence that NSs functions as an essential
573 viral suppressor of RNAi specifically in arthropod cells, revealing distinct mechanistic
574 requirements across host systems.
575 While our immunoprecipitation and computational modeling provide strong evidence
576 for NSs-vsiRNA interactions, quantitative binding parameters remain to be
577 determined. The inherent challenges associated with NSs biochemical
578 characterization, including insolubility during bacterial expression[24,62] and extensive
579 C-terminal disorder that complicates *in vitro* folding, have limited direct binding studies.
580 Despite these technical constraints, our cellular interaction data and structural
581 predictions provide compelling evidence for the RNA-binding capacity and size-
582 specific vsiRNA recognition observed in infected tick cells.
583
584 The convergence of computational predictions, AlphaFold2 structural modeling (Fig.
585 5), and experimental validation reveals that NSs functions through single-strand siRNA
586 sequestration, with discrete binding hotspots that suggest recognition of specific viral

587 RNA secondary structural motifs (Fig. 6, Supplementary Fig. 9). This size-selective
588 mechanism operates at a critical temporal junction, post-Dicer processing, but
589 preceding RISC loading, effectively intercepting single-stranded guide RNAs before
590 Ago2 incorporation. This represents a strategically optimal intervention point that
591 preemptively neutralizes host antiviral responses by depleting the cellular pool of
592 functional guide RNAs. While our data strongly support NSs-mediated sequestration
593 of siRNAs upstream of RISC incorporation, future studies using Ago2
594 immunoprecipitation or RNAi reporter assays will be needed to directly confirm
595 impaired Argonaute loading.
596
597 Importantly, our overlap analysis coupled with molecular docking experiments
598 unambiguously confirms the single-stranded nature of the bound RNA substrates,
599 identifying a previously unrecognized bunyaviral mechanism for RNAi suppression
600 that diverges from canonical dsRNA-binding suppressors. The molecular docking
601 validation using authentic vsiRNA sequences derived from viral infections provides
602 direct structural confirmation and establishes a comprehensive molecular framework
603 for understanding NSs-mediated RNAi evasion. This mechanistic insight represents a
604 substantial functional advancement beyond the previous protein-protein interaction
605 studies (NSs/Ago2) conducted in mammalian cell systems.
606
607 Our findings highlight a key evolutionary adaptation in tick-borne phenuiviruses: the
608 requirement for RNAi suppression in arthropod vectors, but not mammalian hosts. This
609 host-specific dependency likely constrains viral evolution and presents an opportunity
610 for vector-targeted antiviral strategies. The identification of NSs as a siRNA-
611 sequestering protein, rather than an upstream pathway inhibitor, reveals a novel
612 mechanism of immune evasion and offers tractable targets for intervention. Disrupting
613 NSs/vsiRNA interactions or enhancing guide RNA stability could block viral replication
614 in ticks without affecting mammalian infection. While our findings are derived from
615 established tick cell line models, *in vivo* validation in whole *H. logicornis* or *R. microplus*
616 spp. ticks will be essential to confirm the physiological relevance of NSs-mediated
617 RNAi suppression during natural infection. These insights establish NSs as a critical
618 determinant of SFTSV vector competence and uncover a previously unrecognised
619 function for this viral protein.
620

621 # METHODS

622 ## Experimental model and subject detail

623 **Cell culture**
624 Vero E6 cells[63] were cultured in DMEM (Gibco) supplemented with 10% foetal bovine
625 serum (FBS) (Gibco). HuH7-Lunet-T7 cells[64], which stably express T7 RNA
626 polymerase were obtained from R. Bartenschlager, Heidelberg University and were
627 grown in DMEM (Gibco) supplemented with 2 mM L-glutamine, nonessential amino
628 acids, and 10% FBS (Gibco). All mammalian cells were cultured at 37 °C with 5% CO_2.
629 The tick cell lines used in this study were *Amblyomma americanum* AAE2[65] and
630 AAE12[66], *Amblyomma variegatum* AVL/CTVM17[67], *R. microplus* BME/CTVM2[67],
631 BME/CTVM6[67], and BME/CTVM23[68], *R. decoloratus* BDE/CTVM16[67], *H. anatolicum*
632 HAE/CTVM9[69], *Ixodes scapularis* ISE6[70],; *Ixodes ricinus* IRE/CTVM19 and
633 IRE/CTVM20[71] and *Rhipicephalus sanguineus* RML-RSE[72], sourced from the Tick Cell
634 Biobank at the University of Liverpool. The tick cell lines were grown at either 28 °C or
635 32 °C in sealed flat-sided culture tubes (Nunc) containing 2 ml of appropriate complete
636 culture medium (L-15, L-15B, L-15B300, L-15/MEM, L-15/H-Lac, L-15/L-15B or L-
637 15/H-lac/L-15B)[67,73,74] as described previously for maintenance, and transferred to
638 sealed T25 or T80 non-vented flasks to bulk for experimentation. Aag2-AF525 cells,
639 an Ago2 knockout cell line derived from Aag2-AF5 (*Aedes aegypti* mosquito; European
640 Collection of Cell Cultures (ECACC): 19022601) cells by CRISPR/Cas9[11,75] were
641 maintained in Leibovitz's L-15 medium supplemented with 10% FBS (Gibco), 10%
642 tryptose phosphate broth (Gibco), and penicillin-streptomycin (final concentration 100
643 units/ml, 100 µg/ml; Gibco) and maintained at 28 °C.
644
645 **Plasmids**
646 Plasmids for the recovery of SFTSV have been described previously[24,34]. The
647 expression plasmids pTM1-HB29L and pTM1-HB29N contain the SFTSV HB29 L and
648 N ORFs under control of the T7 promoter and encephalomyocarditis virus internal
649 ribosome entry site sequence. The rescue plasmids pTVT7-HB29S, pTVT7-HB29M,
650 and pTVT7-HB29L contain full-length cDNAs of the SFTSV strain HB29 antigenome
651 segments flanked by T7 promoter and hepatitis delta ribozyme sequences. Plasmid
652 pTVT7-HB29SNSsV5 encodes an S segment expressing NSs with a C-terminal V5
653 epitope tag (GKPIPNPLLGLDST). Plasmid pTVT7-HB29SdelNSs:TBSVp19V5
654 encodes an S segment in which the NSs ORF is replaced with the tomato bushy stunt
655 virus p19 protein, also with a C-terminal V5 epitope tag (TBSV; Accession No.
656 M21958.1).
657
658 **Generation of recombinant viruses from cDNA**
659 Recombinant SFTSV were generated by transfecting HuH7-Lunet-T7 cells with 0.1 µg
660 pTM1-HB29L, 0.5 µg pTM1-HB29N, and 1 µg each of pTVT7-based plasmids
661 expressing wt or recombinant viral antigenomic segments. Transfections used 3 µl
662 TransIT-LT1 (Mirus Bio LLC) per µg of DNA as the transfection reagent. After 5 days,
663 transfection supernatants were collected, clarified by low-speed centrifugation, and
664 stored at -80°C. Recombinant virus stocks were amplified in Vero E6 cells at 37 °C by
665 infection at an MOI of 0.01, with culture medium harvested at 7 dpi. The genome
666 segments of recovered viruses were amplified by RT-PCR and sequenced to confirm
667 that no mutations had occurred during the rescue process.
668

669 **Virus Production**
670 SFTSV strains (rHB29pp [wt SFTSV][24] or recombinant viruses rHB2912aaNSs
671 [delNSs][34], rHB29delNSsGFP [delNSs eGFP][34], rHB29NSsV5 [NSsV5] and
672 rHB29delNSsp19V5 [p19V5]) were generated using reverse genetics technologies.
673 The Hubei 29 (HB29) strain is based on a plaque-purified stock called Hubei 29pp
674 (HB29pp) provided by Amy Lambert (CDC Arbovirus Diseases Branch, Fort Collins,
675 CO). Working stocks of SFTSV were generated in Vero E6 cells by infecting at a low
676 multiplicity of infection and harvesting the cell culture medium 7 dpi. Recombinant virus
677 stocks were confirmed by Sanger sequencing to ensure no mutations had occurred
678 during propagation. Previous data have demonstrated that recombinant viruses have
679 the same replication kinetics and viral protein expression profiles as the wt/parental
680 viruses in time course of infection studies[24,34].
681
682 **Virus titration by immunofocus assays**
683 Virus titres were determined by focus-forming assays in Vero E6 cells. Confluent Vero
684 E6 cells were infected with 10-fold serial dilutions of virus prepared in phosphate-
685 buffered saline containing 2% FBS and incubated for 1 h at 37 °C. Following infection,
686 cells were overlaid with MEM supplemented with 2% FBS and 0.6% Avicel (FMC
687 Biopolymer). Cells were incubated for 6 days before fixation and immunostaining as
688 described previously[24].
689

690 **RNA extraction from cell cultures**

691 Total RNA was extracted from cultured cells using 1 ml TRIzol reagent (Thermo Fisher
692 Scientific) according to the manufacturer's protocol. RNA concentrations were
693 measured using a NanoDrop spectrophotometer, and RNA was stored at -80 °C until
694 use.
695

696 **Western blotting**

697 Cell lysates were prepared at indicated timepoints by adding 300 µl lysis buffer (100
698 mM Tris-HCl pH 6.8, 4% SDS, 20% glycerol, 200 mM DTT, 0.2% bromophenol blue,
699 and 25 U/ml Pierce Universal Nuclease [Thermo Fisher]). Proteins were separated on
700 4-12% SDS-polyacrylamide gradient gels (Invitrogen) and transferred to Hybond-C
701 Extra membranes (Amersham). Membranes were blocked in saturation buffer (PBS
702 containing 5% dry milk and 0.1% Tween 20) for 1 h at room temperature. Primary
703 antibodies included SFTSV anti-N or anti-NSs polyclonal rabbit antibodies[24], anti-
704 tubulin monoclonal antibody (Sigma), or anti-V5 antibody (Abcam). After washing,
705 membranes were incubated with goat anti-rabbit DyLight 680 or goat anti-mouse
706 DyLight 800 secondary antibodies (Thermo Fisher). Proteins were visualized using a
707 Li-Cor Odyssey CLx infrared imaging system. Data shown in the manuscript are
708 representative gels from 2-3 independent replicates.
709

710 **Immunofluorescence microscopy**
711 BME/CTVM6 cells previously seeded onto 13mm coverslips for 24 hours were infected
712 with wt or recombinant SFTS viruses at indicated MOIs. At defined timepoints post-
713 infection, cells were fixed with 8% paraformaldehyde in PBS for 15 min at room
714 temperature, permeabilized with 0.5% Triton X-100 for 10 min and blocked with 4%
715 milk in PBS for 1 h. Cells were incubated with primary antibodies overnight at 4 °C,
716 washed 3x with PBS, followed by staining with Alexa Fluor-conjugated secondary

717 antibodies for 1 h at room temperature. Nuclei were counterstained with DAPI (1
718 µg/ml). Images were acquired using a Zeiss LSM 880 confocal microscope and
719 number of nuclei and infection rates quantified using ImageJ (version 1.52p).
720

721 **Northern blotting**

722 BME/CTVM6 or Vero E6 cells were infected with wt SFTSV, and total cellular RNA was
723 extracted at 72 h post-infection using TRIzol reagent (Invitrogen). RNA samples (1 µg)
724 were electrophoresed through 1.2% agarose gels in TAE buffer[76] and transferred via
725 capillary action to positively charged nylon membranes (Roche). Membranes were
726 hybridized with digoxigenin-labelled RNA probes (150 ng each) complementary to
727 negative-sense genomic RNA, positive-sense antigenomic RNA, or subgenomic
728 mRNA sequences encoding N or NSs proteins. Detection was performed using a DIG
729 Northern Starter Kit (Roche) according to the manufacturer's instructions. Data shown
730 in the manuscript are representative gels from 2-3 independent replicates.
731

732 **Small RNA sequencing and library preparation**

733 Total RNA (1 µg per sample) was extracted and processed using the BGI Genomics
734 Small RNA Library Construction Protocol for DNBSEQ platform (DNBSeq, UMI small
735 library, SE50). Following sequential 3' and 5' adaptor ligation, reverse transcription,
736 and PCR amplification (16–17 cycles), libraries were PAGE-purified, circularized to
737 single-stranded DNA, and quality-assessed using an Agilent Bioanalyzer. Sequencing
738 was performed on a DNBSEQ-G400 instrument with 50 bp single-end reads.
739

740 **Small RNA methylation analysis**

741 Methylation status of small RNAs was determined using a beta-elimination assay as
742 previously described[37]. BME/CTVM6 cells (2.5 x 10^5 cells/cm^2) were infected with wt
743 SFTSV (MOI: 0.1) or mock-infected for 3 or 6 days. AF525 cells infected with SFV
744 (MOI: 10, 24 h) served as positive controls for 2'-O-methylation. Following TRIzol LS
745 extraction, RNA samples (200 µl) were treated with 5 µl 20x borate buffer (pH 8.6) and
746 either 12.5 µl 200 mM sodium periodate or nuclease-free water (controls), incubated
747 for 15 min at room temperature, then treated with 10 µl glycerol for an additional 15
748 min. RNA was precipitated overnight at -20 °C using GlycoBlue coprecipitant, 3 M
749 sodium acetate (pH 5.2), and absolute ethanol, recovered by centrifugation (16,000 x
750 g, 15 min, 4 °C), washed with 70% ethanol, and resuspended in 100 µL sodium borate
751 buffer (55 mM, pH 9.5). RNA was purified using the Monarch RNA Cleanup Kit and
752 sequenced by BGI Tech Solutions using DNBSEQ UMI technology (minimum 500 ng
753 input, 20 million clean reads per sample).
754

755 **Small RNA immunoprecipitation assay and RNA extraction**

756 BME/CTVM6 cells were infected with either NSsV5- or p19V5- expressing SFTS
757 viruses (MOI: 1) and cell lysates prepared at 2 dpi to assess viral protein-RNA
758 interactions. Immunoprecipitation was performed using Protein G Dynabeads (Thermo
759 Fisher). Lysis buffer contained 20 mM Tris-HCl pH 7.5, 150 mM NaCl, 5 mM $MgCl_2$,
760 0.5% NP-40, and protease/phosphatase inhibitors (Roche). Wash buffer consisted of
761 50 mM Tris-HCl pH 7.5, 200 mM NaCl, 1 mM EDTA, and 1% NP-40. Dynabeads (20
762 µL) were washed three times, conjugated with 5 µg anti-V5 antibody (Abcam) for 1 h
763 at 4°C, then washed again. Cells were lysed in 100 µL lysis buffer per 10^6 cells for 20

764 min on ice, clarified by centrifugation (16,000 x g, 20 min), and immunoprecipitated
765 overnight at 4 °C with rotation. After three washes, proteins were eluted in LDS buffer
766 at 90 °C for 10 min. For RNA extraction, eluates were treated with proteinase K (1 µg,
767 1 h, 50 °C; Sigma) then processed with TRIzol following standard phenol-chloroform
768 extraction. RNA was precipitated with isopropanol, washed with 75% ethanol, and
769 resuspended in nuclease-free water.
770

771 **Small RNA computational analysis**

772 **Small RNA bioinformatics pipeline**
773 Small RNA libraries (Supplementary Table 4 and 5) were sequenced and processed
774 using a comprehensive bioinformatics pipeline described on the Zenodo repository.
775 Raw sequencing reads were quality-filtered and adapter-trimmed using fastp v0.23[77,78]
776 (1_small_RNA_fastp_processor.sh) with small RNA-optimized parameters: length
777 filtering (18-32 nt), Phred quality score threshold Q20, unqualified base percentage
778 limit 40%, maximum 2 N bases per read, tail trimming with window size 1, poly-G and
779 poly-X trimming enabled, and overrepresentation analysis activated. Adapter
780 sequences were auto detected. FASTA files were standardized and formatted for
781 optimal analysis (2_fasta_formatter.sh).
782

783 **Read alignment and quality control**
784 Reference genome indices were constructed using Bowtie v1.3.1[79,80]
785 (3_bowtie_index_builder.sh), and trimmed reads were aligned to viral (SFTSV HB29
786 strain) and host (*R. microplus* GCA_002176555.1) reference genomes
787 (4_recursive_bowtie_alignment_pipeline_outputs_standspecificBAM.sh,
788 4a_bowtie_stringent_smallRNA_aligner.sh) with stringent parameters: zero
789 mismatches allowed (-v 0), maximum 5 mapping locations per read (-m 5), best
790 alignment reporting (--best --strata), and exhaustive search (--tryhard). Post-alignment
791 filtering retained only uniquely mapping reads with MAPQ ≥20, excluding unmapped
792 (SAM flag 4), secondary (flag 256), and supplementary (flag 2048) alignments. BAM
793 files were strand-separated based on SAM flag 16 (reverse complement) using
794 SAMtools v1.15[81]. Quality filtering statistics and mapping efficiencies were tracked
795 throughout the pipeline to ensure data integrity.
796

797 **Small RNA sequence analysis and characterization**
798 Read length distributions and nucleotide composition analysis were performed using
799 custom scripts (5_Length_Distribution_Analysis.sh) and
800 (5a_strand_specific_Length_Distribution_Analysis.sh) calculating first- and last-base
801 frequencies (A, T/U, G, C percentages) across read lengths 1-50 nt individually, with
802 reads >50 nt grouped. Data transformation for visualization was conducted using R
803 scripts (5_for_generating_length_vs_nt_pc_graph_data.R,
804 5a_for_generating_strand_specific_length_vs_nt_pc_graph_data.R). Chromosome-
805 specific read counting was performed across all BAM files
806 (6_bam_chromosome_read_counter.sh).
807 Coverage analysis employed a custom Python pipeline
808 (7_rpm_normalized_coverage_tool.py) utilizing pysam v0.19.1[82] with CIGAR-aware
809 position counting (equivalent to bedtools -split behaviour) and RPM normalization
810 based on total input reads from original FASTQ files rather than mapped reads. The
811 most abundant small RNA sequences were identified and characterized
812 (9_top_mapping_small_rna_finder.py).

813
814 **Ping-pong amplification analysis**
815 Ping-pong amplification signatures (for vpiRNAs) were detected using a custom
816 algorithm (8_pingpong_smallRNA_analyzer.py) analysing overlapping antisense
817 small RNA pairs within a 1-19 nucleotide window, requiring complementary reads of
818 23-29 nt length with ≥20 nt overlap on opposite strands. The algorithm calculated Z-
819 scores for overlap frequencies and identified statistically significant ping-pong pairs
820 using both raw counts and probability-based H-signatures. Data consolidation across
821 samples was performed (8a_ping_pong_data_consolidator.R) and formatted for
822 analysis (8b_ping_pong_matrix_formatter.R).
823
824 **Small RNA classification**
825 Comprehensive small RNA characterization was conducted using an integrated
826 pipeline (10_small_rna_analysis.py) with configuration management
827 (10a_small_rna_config.yaml, 10b_setup_and_run.sh) that classified small RNA
828 populations as miRNA-like (20-24 nt), siRNA-like (20-25 nt), or piRNA-like (24-32 nt)
829 based on size distribution profiles. All analyses maintained strand-specific resolution
830 with forward strand values reported as positive and reverse strand as negative for
831 visualization.
832

833 **AlphaFold prediction of SFTSV NSs**

834 The sequence of SFTSV NSs (Hubei-29; GenBank ID: AJD86041) was used to query
835 ColabFold's AlphaFold2 structure prediction algorithm using the advanced beta
836 notebook[40,41]. Structure prediction was performed using MMseqs2 for multiple
837 sequence alignment generation, with a maximum MSA depth of 512:1024 sequences
838 and MSA subsampling enabled. Five models were generated with two random seeds
839 each, using 3 recycle iterations and pTM scoring enabled. The ten resulting models
840 were ranked by pLDDT scores, with the highest-ranking model
841 (rank_1_model_5_ptm_seed_0; pLDDT: 72.77, pTMscore: 0.7104) selected for further
842 structural analysis (Supplementary Fig. 5). Subsequent structural analysis was
843 performed using UCSF ChimeraX[83].
844

845 **SFTSV NSs RNA binding prediction**

846 RNA binding prediction for the SFTSV NSs protein sequence was performed using
847 RBDetect[42], a machine learning model trained by Shrinkage Discriminant Analysis
848 (SDA) with a dataset of 8,891 experimentally identified polypeptides from RBDmap
849 experiments, using positive examples (RNA-bound polypeptides) and negative
850 examples (RNA-released polypeptides)[43]. For each amino acid position in the NSs
851 protein sequence, RBDetect assigns a probability value for RNA binding based on the
852 fragment centred at that position. A Hidden Markov model was then used to visualize
853 the probabilities sequentially, determining the most probable RNA binding regions
854 across the protein structure. Predicted RNA binding sites (Supplementary Table 1)
855 were mapped onto the AlphaFold-predicted NSs structure to identify potential
856 functional domains. We also utilised BindUP[84], a computational tool that predicts RNA-
857 binding regions in protein sequences using physicochemical and structural features
858 rather than sequence homology. The tool exploits characteristic surface properties of
859 RNA-binding proteins (RBPs), including electrostatic potential, hydrophobicity, and
860 shape complementarity, to distinguish them from non-RBPs. BindUP employs a

machine-learning framework trained on curated RBP and non-RBP datasets. The software computes surface patches on protein structures (experimental or predicted) and scores their likelihood of mediating RNA interactions[84] (Supplementary Table 2).

RNA secondary structure prediction

RNA secondary structures were predicted using the forna web server (http://rna.tbi.univie.ac.at/forna/, accessed May 2025) powered by the ViennaRNA package[85]. The 76-nucleotide RNA sequence derived from nucleotides 1191-1266 of the antigenomic HB29 S RNA (GenBank: KP202165) was subjected to minimum free energy folding calculations using Turner energy parameters at 37°C. The predicted secondary structure with the lowest free energy was selected for analysis and visualization. No folding constraints were applied during the prediction process.

Modelling of RNA binding to SFTSV NSs

Structural modelling of SFTSV NSs-vsiRNA interactions was performed using AlphaFold3. The SFTSV NSs protein sequence (Hubei-29; GenBank ID: AJD86041) was submitted to the AlphaFold3 webserver (version 2.0) with representative 22-nucleotide vsiRNA sequences identified from NSs immunoprecipitation experiments in SFTSV-infected BME/CTVM6 tick cells. vsiRNA sequences were selected based on abundance in NSs-IP samples from identified hotspots within each viral RNA segment (Supplementary Table 3). Five independent structural predictions were generated for each NSs-vsiRNA complex using default parameters. Models were selected based on per-residue confidence scores (pLDDT >70 for NSs functional domains) and interface confidence scores (>0.5 for protein-RNA contacts). Structural analysis was performed using UCSF ChimeraX (version 1.6)[83], focusing on RNA-binding interfaces, contact residues within 4 Å of vsiRNA substrates, and structural determinants of vsiRNA recognition (Supplementary Table 6).

Proteomic analysis

To estimate relative abundance of SFTSV proteins, we analyzed proteomic data from project PXD054068, which comprises whole-cell proteomes of BME/CTVM6 tick cells infected with SFTSV (MOI 1) at 3- and 6-dpi with four biological replicates. Corresponding peptides for each viral protein [non-structural protein (NSs; AJD86041), nucleocapsid protein (N; AJD86040), glycoprotein precursor (GPC; AJD86039) or RNA-dependent RNA polymerase (RdRp; AJD86038)] were pooled across replicates at each time point, and peptide intensity distributions were analyzed. Scripts used to generate plots and statistics are available from the Zenodo online repository (https://doi.org/10.5281/zenodo.15877198). Statistical significance of changes in peptide intensities between time points was assessed using Welch's t-test.

Biosafety

All experiments with infectious SFTSV were performed in the Richard Elliott Biosafety Laboratories (REBL) at the MRC-University of Glasgow Centre for Virus Research, under containment level 3 (CL-3) conditions, approved by the UK Health and Safety Executive (GM223/20.2a).

Quantification and Statistical Analysis

Experiments were performed with a minimum of n=2 biological replicates unless otherwise stated, with each biological sample tested in technical replicates where applicable. Technical replicates were averaged before statistical analysis. Data are presented as mean ± SD e.g. for virus titres and cell counts. For immunofluorescence quantification, n=3 randomised fields of view were analysed per condition. Small RNA sequencing experiments used n=3 biologically independent samples. Statistical significance for multiple group comparisons was assessed using Brown-Forsythe and Welch's ANOVA with Dunnett's T3 multiple comparison test. Statistical significance was set at $p \leq 0.05$, with * $p \leq 0.05$, ** $p \leq 0.01$; 'ns' indicates not significant. Individual sample sizes are indicated in figure legends. Statistical analyses were performed using GraphPad Prism Version 10.5.0 (673).

ACKNOWLEDGEMENTS

We thank Prof. Ulrike Munderloh, University of Minnesota, for permission to use the ISE6, AAE2 and AAE12 cell lines. We also thank Dr Matthew Arnold (Royal Veterinary College) for support with the initial AlphaFold modelling.

FUNDING

This research was funded by a Wellcome Trust/Royal Society Sir Henry Dale Fellowship (210462/Z/18/Z) awarded to B.B. (supporting M.F., M.McF., K.D., A.T.C and B.B.). The facilities used in this study were funded by the UK Medical Research Council (MC_UU_00034/4, MC_UU_00034/8). R.H.P. was supported by a Medical Research Future Fund, Early to Mid-Career Researcher Grant MRF2022950. L.B.S. was supported by the UK BBSRC grant no. BB/P024270/1 and the Wellcome Trust grant no. 223743/Z/21/Z. M.J.P. was funded by European Union's Horizon 2020 Research and Innovation Program under the Marie Skłodowska-Curie grant agreement No 890970. E.S. was funded by German Centre for Infection Research (DZIF) (TTU 01.708). A.C. is funded by the European Research Council (ERC) Consolidator Grant 'vRNP-capture' 101001634 and the MRC grants MR/R021562/1 and MC_UU_00034/2 (supporting R.A & W.K.). A.K., was funded by the UK Medical Research Council (MC_UU_12014/8, MC_UU_00034/4). This research was funded in whole or in part by the Wellcome Trust.

The funders had no role in study design, data collection and analysis, decision to publish, or preparation of the manuscript.

AUTHORS' CONTRIBUTIONS

Conceptualization: M.F., M.McF., E.S., A.C., A.K., B.B., Data Curation: M.F., M.McF., R.H.P., R.A., A.T.C., M.P., B.B., Formal Analysis: M.F., M.McF., R.H.P., R.A., A.T.C., W.K., M.P., A.C., A.K., B.B., Funding Acquisition: B.B., Investigation: M.F., M.McF., R.H.P., R.A., A.T.C., W.K., K.D., A.C., A.K., B.B., Methodology: M.F., M.McF., R.H.P., M.P., E.S., B.B., Project administration: B.B., Resources: L.B.S., B.B., Software: R.H.P., B.B., Supervision: A.C., A.K., B.B., Validation: M.F., M.McF., R.H.P., R.A., A.T.C., W.K., K.D., M.P., E.S., A.C., A.K., B.B., Visualization: M.F., M.McF., R.H.P.,

R.A., A.T.C., W.K., B.B., Writing – original draft: M.F., M.McF., A.K., B.B., Writing – review & editing: M.F., M.McF., R.H.P., R.A., A.T.C., W.K., K.D., L.B.S., M.P., E.S., A.C., A.K., B.B.

DECLARATION OF INTERESTS

The authors declare no competing interests.

DATA AVAILABILITY

All data that support the findings of this study are openly available from Enlighten Research Data (https://doi.org/10.5525/gla.researchdata.2028). All sequencing data generated in this study have been deposited in the NCBI Sequence Read Archive under BioProject accession number PRJNA1283909. The bioinformatic scripts used for analysis can be found in the Zenodo online repository (https://doi.org/10.5281/zenodo.15877198).

REFERENCES

1 Yu, X. J. *et al.* Fever with thrombocytopenia associated with a novel bunyavirus in China. *N Engl J Med* **364**, 1523-1532 (2011). https://doi.org:10.1056/NEJMoa1010095

2 Casel, M. A., Park, S. J. & Choi, Y. K. Severe fever with thrombocytopenia syndrome virus: emerging novel phlebovirus and their control strategy. *Exp Mol Med* **53**, 713-722 (2021). https://doi.org:10.1038/s12276-021-00610-1

3 Li, J. C., Zhao, J., Li, H., Fang, L. Q. & Liu, W. Epidemiology, clinical characteristics, and treatment of severe fever with thrombocytopenia syndrome. *Infect Med (Beijing)* **1**, 40-49 (2022). https://doi.org:10.1016/j.imj.2021.10.001

4 Jang, H. *et al.* Seasonal dynamics of Haemaphysalis tick species as SFTSV vectors in South Korea. *Microbiol Spectr* **12**, e0048924 (2024). https://doi.org:10.1128/spectrum.00489-24

5 Hu, Y. Y. *et al.* Role of three tick species in the maintenance and transmission of Severe Fever with Thrombocytopenia Syndrome Virus. *PLoS Negl Trop Dis* **14**, e0008368 (2020). https://doi.org:10.1371/journal.pntd.0008368

6 Pérez, L. J., Baele, G., Hong, S. L., Cloherty, G. A. & Berg, M. G. Ecological Changes Exacerbating the Spread of Invasive Ticks has Driven the Dispersal of Severe Fever with Thrombocytopenia Syndrome Virus Throughout Southeast Asia. *Mol Biol Evol* **41** (2024). https://doi.org:10.1093/molbev/msae173

7 Barry, G. *et al.* Gene silencing in tick cell lines using small interfering or long double-stranded RNA. *Exp Appl Acarol* **59**, 319-338 (2013). https://doi.org:10.1007/s10493-012-9598-x

8 Schnettler, E. *et al.* Induction and suppression of tick cell antiviral RNAi responses by tick-borne flaviviruses. *Nucleic Acids Res* **42**, 9436-9446 (2014). https://doi.org:10.1093/nar/gku657

9 Hoffmann, H. H., Schneider, W. M. & Rice, C. M. Interferons and viruses: an evolutionary arms race of molecular interactions. *Trends Immunol* **36**, 124-138 (2015). https://doi.org:10.1016/j.it.2015.01.004

10 Gammon, D. B. & Mello, C. C. RNA interference-mediated antiviral defense in insects. *Curr Opin Insect Sci* **8**, 111-120 (2015). https://doi.org:10.1016/j.cois.2015.01.006

11 Scherer, C. *et al.* An Aedes aegypti-Derived Ago2 Knockout Cell Line to Investigate Arbovirus Infections. *Viruses* **13** (2021). https://doi.org:10.3390/v13061066

12 Horwich, M. D. *et al.* The Drosophila RNA methyltransferase, DmHen1, modifies germline piRNAs and single-stranded siRNAs in RISC. *Curr Biol* **17**, 1265-1272 (2007). https://doi.org:10.1016/j.cub.2007.06.030

13 Yang, Z., Vilkaitis, G., Yu, B., Klimasauskas, S. & Chen, X. Approaches for studying microRNA and small interfering RNA methylation in vitro and in vivo. *Methods Enzymol* **427**, 139-154 (2007). https://doi.org:10.1016/S0076-6879(07)27008-9

14 Alefelder, S., Patel, B. K. & Eckstein, F. Incorporation of terminal phosphorothioates into oligonucleotides. *Nucleic Acids Res* **26**, 4983-4988 (1998). https://doi.org:10.1093/nar/26.21.4983

15 Elmer, K., Helfer, S., Mirkovic-Hosle, M. & Forstemann, K. Analysis of endo-siRNAs in Drosophila. *Methods Mol Biol* **1173**, 33-49 (2014). https://doi.org:10.1007/978-1-4939-0931-5_4
16 Blair, C. D. & Olson, K. E. The role of RNA interference (RNAi) in arbovirus-vector interactions. *Viruses* **7**, 820-843 (2015). https://doi.org:10.3390/v7020820
17 Wilson, A. *et al.* Uukuniemi virus infection causes a pervasive remodelling of the RNA-binding proteome in tick cells. *PLoS Pathog* **21**, e1013393 (2025). https://doi.org:10.1371/journal.ppat.1013393
18 Song, L. *et al.* Silencing suppressors: viral weapons for countering host cell defenses. *Protein Cell* **2**, 273-281 (2011). https://doi.org:10.1007/s13238-011-1037-y
19 van Mierlo, J. T. *et al.* Novel Drosophila viruses encode host-specific suppressors of RNAi. *PLoS Pathog* **10**, e1004256 (2014). https://doi.org:10.1371/journal.ppat.1004256
20 Hedil, M. & Kormelink, R. Viral RNA Silencing Suppression: The Enigma of Bunyavirus NSs Proteins. *Viruses* **8** (2016). https://doi.org:10.3390/v8070208
21 Blakqori, G. *et al.* La Crosse bunyavirus nonstructural protein NSs serves to suppress the type I interferon system of mammalian hosts. *J Virol* **81**, 4991-4999 (2007). https://doi.org:10.1128/jvi.01933-06
22 Xu, Y. *et al.* Antiviral RNA interference in disease vector (Asian longhorned) ticks. *PLoS Pathog* **17**, e1010119 (2021). https://doi.org:10.1371/journal.ppat.1010119
23 Javaid, N., Jang, T. W., Fu, Y. & Choi, Y. SFTSV NSs interacts with AGO2 to regulate the RNAi pathway for viral replication. *J Virol* **99**, e0220524 (2025). https://doi.org:10.1128/jvi.02205-24
24 Brennan, B. *et al.* Reverse genetics system for severe fever with thrombocytopenia syndrome virus. *J Virol* **89**, 3026-3037 (2015). https://doi.org:10.1128/jvi.03432-14
25 Mazelier, M. *et al.* Uukuniemi Virus as a Tick-Borne Virus Model. *J Virol* **90**, 6784-6798 (2016). https://doi.org:10.1128/jvi.00095-16
26 Reynolds, E. S., Wooldridge, J. T., Stevenson, H. L. & Thangamani, S. The Lone Star tick, Amblyomma americanum, salivary factors exacerbate the clinical outcome of Heartland virus disease in a small animal model. *Sci Rep* **13**, 13304 (2023). https://doi.org:10.1038/s41598-023-40397-x
27 McMullan, L. K. *et al.* A new phlebovirus associated with severe febrile illness in Missouri. *N Engl J Med* **367**, 834-841 (2012). https://doi.org:10.1056/NEJMoa1203378
28 Salvati, M. V. *et al.* Virus-Derived DNA Forms Mediate the Persistent Infection of Tick Cells by Hazara Virus and Crimean-Congo Hemorrhagic Fever Virus. *J Virol* **95**, e0163821 (2021). https://doi.org:10.1128/jvi.01638-21
29 Petit, M. J. *et al.* Multi-omics analysis of SFTS virus infection in Rhipicephalus microplus cells reveals antiviral tick factors. *Nat Commun* **16**, 4732 (2025). https://doi.org:10.1038/s41467-025-59565-w
30 Rezelj, V. V. *et al.* Differential Antagonism of Human Innate Immune Responses by Tick-Borne Phlebovirus Nonstructural Proteins. *mSphere* **2** (2017). https://doi.org:10.1128/mSphere.00234-17
31 Bryden, S. R. *et al.* Exploration of immunological responses underpinning severe fever with thrombocytopenia syndrome virus infection reveals IL-6 as a

therapeutic target in an immunocompromised mouse model. *PNAS Nexus* **1**, pgac024 (2022). https://doi.org:10.1093/pnasnexus/pgac024

32 Yu, K. M. *et al.* Cross-genotype protection of live-attenuated vaccine candidate for severe fever with thrombocytopenia syndrome virus in a ferret model. *Proc Natl Acad Sci U S A* **116**, 26900-26908 (2019). https://doi.org:10.1073/pnas.1914704116

33 Choi, Y. *et al.* Severe fever with thrombocytopenia syndrome phlebovirus non-structural protein activates TPL2 signalling pathway for viral immunopathogenesis. *Nat Microbiol* **4**, 429-437 (2019). https://doi.org:10.1038/s41564-018-0329-x

34 Brennan, B., Rezelj, V. V. & Elliott, R. M. Mapping of Transcription Termination within the S Segment of SFTS Phlebovirus Facilitated Generation of NSs Deletant Viruses. *J Virol* **91** (2017). https://doi.org:10.1128/jvi.00743-17

35 Elliott, R. M. & Brennan, B. Emerging phleboviruses. *Curr Opin Virol* **5**, 50-57 (2014). https://doi.org:10.1016/j.coviro.2014.01.011

36 Reuter, M. *et al.* The PAZ domain of Aedes aegypti Dicer 2 is critical for accurate and high-fidelity size determination of virus-derived small interfering RNAs. *RNA* **31**, 679-691 (2025). https://doi.org:10.1261/rna.080149.124

37 Yang, Z., Ebright, Y. W., Yu, B. & Chen, X. HEN1 recognizes 21-24 nt small RNA duplexes and deposits a methyl group onto the 2' OH of the 3' terminal nucleotide. *Nucleic Acids Res* **34**, 667-675 (2006). https://doi.org:10.1093/nar/gkj474

38 Canto, T., Uhrig, J. F., Swanson, M., Wright, K. M. & MacFarlane, S. A. Translocation of Tomato bushy stunt virus P19 protein into the nucleus by ALY proteins compromises its silencing suppressor activity. *J Virol* **80**, 9064-9072 (2006). https://doi.org:10.1128/JVI.00953-06

39 Park, J. W., Faure-Rabasse, S., Robinson, M. A., Desvoyes, B. & Scholthof, H. B. The multifunctional plant viral suppressor of gene silencing P19 interacts with itself and an RNA binding host protein. *Virology* **323**, 49-58 (2004). https://doi.org:10.1016/j.virol.2004.02.008

40 Jumper, J. *et al.* Highly accurate protein structure prediction with AlphaFold. *Nature* **596**, 583-589 (2021). https://doi.org:10.1038/s41586-021-03819-2

41 Varadi, M. *et al.* AlphaFold Protein Structure Database: massively expanding the structural coverage of protein-sequence space with high-accuracy models. *Nucleic Acids Res* **50**, D439-d444 (2022). https://doi.org:10.1093/nar/gkab1061

42 Kamel, W. *et al.* Global analysis of protein-RNA interactions in SARS-CoV-2-infected cells reveals key regulators of infection. *Mol Cell* **81**, 2851-2867.e2857 (2021). https://doi.org:10.1016/j.molcel.2021.05.023

43 Castello, A. *et al.* Comprehensive Identification of RNA-Binding Domains in Human Cells. *Mol Cell* **63**, 696-710 (2016). https://doi.org:10.1016/j.molcel.2016.06.029

44 Paz, I., Kligun, E., Bengad, B. & Mandel-Gutfreund, Y. BindUP: a web server for non-homology-based prediction of DNA and RNA binding proteins. *Nucleic Acids Res.* **44**, W568-W574 (2016). https://doi.org:10.1093/NAR/GKW454

45 Silhavy, D. *et al.* A viral protein suppresses RNA silencing and binds silencing-generated, 21- to 25-nucleotide double-stranded RNAs. *EMBO J* **21**, 3070-3080 (2002). https://doi.org:10.1093/emboj/cdf312

46 Léger, P. *et al.* Dicer-2- and Piwi-mediated RNA interference in Rift Valley fever virus-infected mosquito cells. *J Virol* **87**, 1631-1648 (2013). https://doi.org:10.1128/jvi.02795-12

47 Brennan, B., Welch, S. R. & Elliott, R. M. The consequences of reconfiguring the ambisense S genome segment of Rift Valley fever virus on viral replication in mammalian and mosquito cells and for genome packaging. *PLoS Pathog* **10**, e1003922 (2014). https://doi.org:10.1371/journal.ppat.1003922

48 Brault, A. C., Savage, H. M., Duggal, N. K., Eisen, R. J. & Staples, J. E. Heartland Virus Epidemiology, Vector Association, and Disease Potential. *Viruses* **10** (2018). https://doi.org:10.3390/v10090498

49 Lara, E., Billecocq, A., Leger, P. & Bouloy, M. Characterization of wild-type and alternate transcription termination signals in the Rift Valley fever virus genome. *J Virol* **85**, 12134-12145 (2011). https://doi.org:10.1128/jvi.05322-11

50 Moutailler, S., Krida, G., Madec, Y., Bouloy, M. & Failloux, A. B. Replication of Clone 13, a naturally attenuated avirulent isolate of Rift Valley fever virus, in Aedes and Culex mosquitoes. *Vector Borne Zoonotic Dis* **10**, 681-688 (2010). https://doi.org:10.1089/vbz.2009.0246

51 Moutailler, S. *et al.* Host alternation is necessary to maintain the genome stability of rift valley fever virus. *PLoS Negl Trop Dis* **5**, e1156 (2011). https://doi.org:10.1371/journal.pntd.0001156

52 Geiger, T. *et al.* Use of stable isotope labeling by amino acids in cell culture as a spike-in standard in quantitative proteomics. *Nat Protoc* **6**, 147-157 (2011). https://doi.org:10.1038/nprot.2010.192

53 Schwanhausser, B. *et al.* Global quantification of mammalian gene expression control. *Nature* **473**, 337-342 (2011). https://doi.org:10.1038/nature10098

54 Vargason, J. M., Szittya, G., Burgyán, J. & Hall, T. M. Size selective recognition of siRNA by an RNA silencing suppressor. *Cell* **115**, 799-811 (2003). https://doi.org:10.1016/s0092-8674(03)00984-x

55 Shalamova, L. *et al.* Nucleocapsids of the Rift Valley fever virus ambisense S segment contain an exposed RNA element in the center that overlaps with the intergenic region. *Nature Communications* **15**, 7602 (2024). https://doi.org:10.1038/s41467-024-52058-2

56 Blair, C. D. Deducing the Role of Virus Genome-Derived PIWI-Associated RNAs in the Mosquito-Arbovirus Arms Race. *Front Genet* **10**, 1114 (2019). https://doi.org:10.3389/fgene.2019.01114

57 Rückert, C. *et al.* Small RNA responses of Culex mosquitoes and cell lines during acute and persistent virus infection. *Insect Biochem Mol Biol* **109**, 13-23 (2019). https://doi.org:10.1016/j.ibmb.2019.04.008

58 Dietrich, I. *et al.* RNA Interference Restricts Rift Valley Fever Virus in Multiple Insect Systems. *mSphere* **2** (2017). https://doi.org:10.1128/mSphere.00090-17

59 Dietrich, I. *et al.* The Antiviral RNAi Response in Vector and Non-vector Cells against Orthobunyaviruses. *PLoS Negl Trop Dis* **11**, e0005272 (2017). https://doi.org:10.1371/journal.pntd.0005272

60 Eifan, S., Schnettler, E., Dietrich, I., Kohl, A. & Blomström, A. L. Non-structural proteins of arthropod-borne bunyaviruses: roles and functions. *Viruses* **5**, 2447-2468 (2013). https://doi.org:10.3390/v5102447

61 Schnettler, E. *et al.* Diverging affinity of tospovirus RNA silencing suppressor proteins, NSs, for various RNA duplex molecules. *J Virol* **84**, 11542-11554 (2010). https://doi.org:10.1128/jvi.00595-10

62 Tao, X. *et al.* Preparation of a polyclonal antibody against the non-structural protein, NSs of SFTSV. *Protein Expr Purif* **184**, 105892 (2021). https://doi.org:10.1016/j.pep.2021.105892

63 Billecocq, A., Vialat, P. & Bouloy, M. Persistent infection of mammalian cells by Rift Valley fever virus. *J Gen Virol* **77 (Pt 12)**, 3053-3062 (1996). https://doi.org:10.1099/0022-1317-77-12-3053

64 Kaul, A., Woerz, I., Meuleman, P., Leroux-Roels, G. & Bartenschlager, R. Cell culture adaptation of hepatitis C virus and in vivo viability of an adapted variant. *J. Virol.* **81**, 13168-13179 (2007). https://doi.org:10.1128/jvi.01362-07

65 Kurtti, T. J., Simser, J. A., Baldridge, G. D., Palmer, A. T. & Munderloh, U. G. Factors influencing in vitro infectivity and growth of Rickettsia peacockii (Rickettsiales: Rickettsiaceae), an endosymbiont of the Rocky Mountain wood tick, Dermacentor andersoni (Acari, Ixodidae). *J Invertebr Pathol* **90**, 177-186 (2005). https://doi.org:10.1016/j.jip.2005.09.001

66 Singu, V. *et al.* Unique macrophage and tick cell-specific protein expression from the p28/p30-outer membrane protein multigene locus in Ehrlichia chaffeensis and Ehrlichia canis. *Cell Microbiol* **8**, 1475-1487 (2006). https://doi.org:10.1111/j.1462-5822.2006.00727.x

67 Bell-Sakyi, L. Ehrlichia ruminantium grows in cell lines from four ixodid tick genera. *J Comp Pathol* **130**, 285-293 (2004). https://doi.org:10.1016/j.jcpa.2003.12.002

68 Alberdi, M. P., Nijhof, A. M., Jongejan, F. & Bell-Sakyi, L. Tick cell culture isolation and growth of Rickettsia raoultii from Dutch Dermacentor reticulatus ticks. *Ticks Tick Borne Dis* **3**, 349-354 (2012). https://doi.org:10.1016/j.ttbdis.2012.10.020

69 Bell-Sakyi, L. Continuous cell lines from the tick Hyalomma anatolicum anatolicum. *J Parasitol* **77**, 1006-1008 (1991).

70 Kurtti, T. J., Munderloh, U. G., Andreadis, T. G., Magnarelli, L. A. & Mather, T. N. Tick cell culture isolation of an intracellular prokaryote from the tick Ixodes scapularis. *J Invertebr Pathol* **67**, 318-321 (1996). https://doi.org:10.1006/jipa.1996.0050

71 Bell-Sakyi, L., Zweygarth, E., Blouin, E. F., Gould, E. A. & Jongejan, F. Tick cell lines: tools for tick and tick-borne disease research. *Trends Parasitol* **23**, 450-457 (2007). https://doi.org:10.1016/j.pt.2007.07.009

72 Yunker, C. E., Cory, J. & Meibos, H. Continuous cell lines from embryonic tissues of ticks (Acari: Ixodidae). *In Vitro* **17**, 139-142 (1981). https://doi.org:10.1007/bf02618071

73 Munderloh, U. G. & Kurtti, T. J. Formulation of medium for tick cell culture. *Exp Appl Acarol* **7**, 219-229 (1989). https://doi.org:10.1007/bf01194061

74 Munderloh, U. G. *et al.* Invasion and intracellular development of the human granulocytic ehrlichiosis agent in tick cell culture. *J Clin Microbiol* **37**, 2518-2524 (1999). https://doi.org:10.1128/jcm.37.8.2518-2524.1999

75 Fredericks, A. C. *et al.* Aedes aegypti (Aag2)-derived clonal mosquito cell lines reveal the effects of pre-existing persistent infection with the insect-specific bunyavirus Phasi Charoen-like virus on arbovirus replication. *PLoS Negl Trop Dis* **13**, e0007346 (2019). https://doi.org:10.1371/journal.pntd.0007346

76 Masek, T., Vopalensky, V., Suchomelova, P. & Pospisek, M. Denaturing RNA electrophoresis in TAE agarose gels. *Anal Biochem* **336**, 46-50 (2005). https://doi.org:S0003-2697(04)00732-8 [pii]
10.1016/j.ab.2004.09.010

77 Chen, S. Ultrafast one-pass FASTQ data preprocessing, quality control, and deduplication using fastp. *iMeta* **2**, e107 (2023). https://doi.org:10.1002/imt2.107

78 Chen, S., Zhou, Y., Chen, Y. & Gu, J. fastp: an ultra-fast all-in-one FASTQ preprocessor. *Bioinformatics* **34**, i884-i890 (2018). https://doi.org:10.1093/bioinformatics/bty560

79 Langmead, B. Aligning short sequencing reads with Bowtie. *Current Protocols in Bioinformatics* **Chapter 11**, Unit 11.17 (2010). https://doi.org:10.1002/0471250953.bi1107s32

80 Langmead, B., Trapnell, C., Pop, M. & Salzberg, S. L. Ultrafast and memory-efficient alignment of short DNA sequences to the human genome. *Genome Biology* **10**, R25 (2009). https://doi.org:10.1186/gb-2009-10-3-r25

81 Li, H. *et al.* The Sequence Alignment/Map format and SAMtools. *Bioinformatics* **25**, 2078-2079 (2009). https://doi.org:10.1093/bioinformatics/btp352

82 pysam: Python interface for SAM/BAM sequence alignment and mapping format (GitHub, 2009).

83 Goddard, T. D. *et al.* UCSF ChimeraX: Meeting modern challenges in visualization and analysis. *Protein Sci* **27**, 14-25 (2018). https://doi.org:10.1002/pro.3235

84 Paz, I., Kligun, E., Bengad, B. & Mandel-Gutfreund, Y. BindUP: a web server for non-homology-based prediction of DNA and RNA binding proteins. *Nucleic Acids Res* **44**, W568-574 (2016). https://doi.org:10.1093/nar/gkw454

85 Lorenz, R. *et al.* ViennaRNA Package 2.0. *Algorithms for Molecular Biology* **6**, 26 (2011). https://doi.org:10.1186/1748-7188-6-26

FIGURE LEGENDS

Fig. 1. Initial characterisation of wt SFTSV replication in a diverse range of tick cells.

(A) Titre of wt SFTSV in the supernatant of infected tick cells (MOI: 1) assayed at 10 dpi. Cell lines used were derived from tick genera (*, grey) *Amblyomma* (#, purple) *Hyalomma* ($, blue) *Rhipicephalus* or (&, pink) *Ixodes.* Dashed line represents titre of initial inoculum. Data are plotted as virus titre (FFU/ml) and show a representative experiment of n=2 biological replicates.

(B) Representative images of cell extracts derived from cell monolayers in **(A)**. Western blots were probed with anti-tubulin (loading control) or anti-SFTSV N antibodies to detect cellular and viral protein expression.

(C) Tick cell lines derived from *Rhipicephalus microplus* or *Ixodes* spp. were infected with wt SFTSV (MOI: 0.1) for up to 10 dpi. Data are plotted as virus titre (FFU/ml) and show n=1 experiment.

(D) At 10 dpi, wt SFTSV-infected tick cell cultures described in **(C)** were passaged and split (1:2) and left to recover for a minimum of 14 days. This process was repeated for up to 3 subsequent passages. Data are plotted as virus titre (FFU/ml) and show a representative experiment (n=1).

(E-F) Titre of **(E)** wt or **(F)** delNSs SFTSV in the supernatant of infected BME/CTVM6 cells (MOI: 0.1 [grey]; 1 [blue]; or 5 [red]) assayed at the indicated timepoints p.i. Data are plotted as the mean virus titre (FFU/ml) ± SD of n=2 biological replicates.

(G) Representative images of cell lysates derived from cell monolayers in **(E)** and **(F)** harvested at 72 h p.i. As a control, Vero E6 cells were infected with wt SFTSV (MOI: 1) and cell lysates were prepared at 72 h p.i. Western blots were probed with anti-tubulin (loading control), anti-SFTSV NSs or anti-SFTSV N antibodies to detect cellular and viral protein expression. '-ve': mock-infected cell lysate, 'wt': wt SFTSV infected cell lysate, 'delNSs': delNSs SFTSV infected cell lysate. Data show a representative experiment (n=3).

(H) BME/CTVM6 cells seeded onto coverslips were infected with wt- or delNSs- SFTSV at the indicated MOI and were imaged at the timepoints indicated using DAPI (blue) and anti-SFTSV N (red). Imaging was carried out using a Zeiss LSM 880 Confocal Microscope, scale bar is equal to 50 µm.

(I) Percentage of BME/CTVM6 cells infected with delNSs SFTSV (MOI: 0.1 [grey]; 1 [blue]; or 5 [red]) at the timepoints indicated, evidenced by positive staining with anti-SFTSV N antibody. Data are plotted as the mean percent SFTSV-positive cells ± SD of n=3 randomised fields of view.

(J) Number of nuclei enumerated per field of view in (I). Data are plotted as the mean number of nuclei observed ± SD of n=3 randomised fields of view.

(K) Percentage of BME/CTVM6 cells infected with wt SFTSV (MOI: 0.1 [grey]; 1 [blue]; or 5 [red]) at the timepoints indicated, evidenced by positive staining with anti-SFTSV N antibody. Data are plotted as the mean percent SFTSV-positive cells ± SD of n=3 randomised fields of view.

(L) Number of nuclei enumerated per field of view in (K). Data are plotted as the mean number of nuclei observed ± SD of n=3 randomised fields of view.

(M) Violin plot showing peptide intensity distributions (y-axis: Log_2) for wt SFTSV-infected BME/CTVM6 cells at 3- and 6-dpi. Examining peptides derived from non-structural protein (NSs; AJD86041), nucleocapsid protein (N; AJD86040), glycoprotein precursor (GPC; AJD86039) or RNA-dependent RNA polymerase (RdRp; AJD86038). Data taken from n=4 biologically independent replicates.

(N) Bar Chart showing mean peptide intensities (y-axis: Log_2) for same data set presented in (M).

(O) Schematic of SFTSV S genomic RNA configuration showing DIG-labelled probe binding regions used in (P). Probes detect viral genomic (−) or antigenomic (+) sense RNA as indicated. Double-ended arrows indicate genomic replication; single-ended arrows indicate transcription. Black circles indicate 5′ cap structures on mRNAs.

(P) Northern blot analysis of viral RNAs in infected cells. BME/CTVM6 and BME/CTVM23 cells were infected with wt SFTSV (MOI: 0.1) and total RNA was extracted at 6 dpi. Vero E6 cells infected with wt SFTSV were used as a positive control (RNA extracted at 72 h p.i.). DIG-labelled probes complementary to N or NSs coding sequences detected viral genomic (−) or antigenomic (+) sense RNAs. RNA sizes are indicated on the right.

Fig. 2. BME/CTVM6 cells produce virus derived siRNAs upon wt SFTSV infection.

BME/CTVM6 cells were infected with wt SFTSV (MOI: 0.1) and total cellular RNA was extracted from infected cells at 3 (light shade) or 6 (dark shade) dpi. Following RNA extraction, samples were either left untreated or processed in a beta-elimination assay, then subjected to small RNA sequencing.

(A) Total number of small RNA reads (18-30 nt) in infected cells at 3 (light shading) and 6 (dark shading) dpi. mapping to each wt SFTSV genome segment in untreated samples (left) or beta-eliminated samples (right). SFTSV genome segments: S (KP202165), M (KP202164), L (KP202163).

(B) Histogram of all small RNA reads (18-30nt) from from untreated (left) or beta-eliminated (right) samples from infected cells at 3 dpi. Read counts are coloured by the identity of the 5′ nucleotide and grouped by read length. Data are shown as the mean percentage of total mapped reads (y-axis); representative of n=3 biologically independent samples.

(C) As per (B), but RNAs were extracted from wt SFTSV-infected cells at 6 dpi.

(D) Histogram of small RNA reads (18-30 nt) from untreated (left) or beta-eliminated (right) samples, mapped to the combined SFTSV antigenomic (positive values) and genomic (negative values) strand RNAs in infected cells at 3 dpi. Read counts are coloured by the identity of the 5′ nucleotide and grouped by read length. Data are shown as the mean percentage of total mapped reads (y-axis); representative of n=3 biologically independent samples.

(E) As per (D), but RNAs were extracted from wt SFTSV-infected cells at 6 dpi.

(F-H) Mapping of SFTSV-derived 22 nt vsiRNAs (reads per million) across the **(F)** S, **(G)** M, and **(H)** L genome segments at 3 (left) and 6 (right) dpi in BME/CTVM6 cells. Data show antigenomic (blue) and genomic (pink) sense strands for untreated (top) or beta-eliminated samples (bottom) to remove 2'-O-methylated small RNAs. Numbers indicate nucleotide positions (nt). SFTSV genome segments: S (KP202165), M (KP202164), L (KP202163). Dashed lines represent the boundaries of viral open reading frames and untranslated/intergenic regions.

Fig. 3. SFTSV vsiRNAs exhibit canonical n-2 Dicer processing signature.
Reanalysis of data from Fig. 2.
(A,C) Distribution of overlapping 22 nt vsiRNA pairs by nucleotide overlap length across S (left), M (middle), and L (right) genome segments (normalized per million mapped SFTSV reads).
(B,D) Heat maps showing overlap probability z-scores for vsiRNAs of different lengths (x-axis) and overlap positions (y-axis) from three independent samples. Black boxes highlight the characteristic 2 nt overlap signature of Dicer-2 processing. Colour scale represents z-score values from -4 (teal) to +4 (purple).
(A,B) data from 3 dpi. and **(C,D)** data from 6 dpi.

Fig. 4. TBSV p19 protein rescues delNSs SFTSV replication in BME/CTVM6 cells.
BME/CTVM6 cells infected with **(A)** wt SFTSV or **(B)** delNSs-eGFP virus (MOI: 0.1). At 6 dpi, cells were fixed and immunostained for SFTSV N protein (red) and nuclei (DAPI, blue). **(C)** Western blot analysis of viral protein expression in infected BME/CTVM6 cells (6 dpi) and control Vero E6 cells (72 h p.i., MOI: 1). Blots were probed with antibodies against tubulin (loading control), SFTSV NSs, SFTSV N, or V5 tag. Lane labels: wt, wild-type SFTSV; G, delNSs-eGFP; p19, delNSs-p19V5. **(D,E)** BME/CTVM6 cells infected with delNSs-p19V5 virus (MOI: 10). Panel E shows higher magnification of infected cells. **(F)** Viral replication kinetics in BME/CTVM6 cells infected with wt SFTSV (teal), delNSs-p19V5 (red), or delNSs-eGFP (black) viruses. Virus titres were determined by focus-forming assay at indicated time points. Data show one representative experiment from n=3 independent repeats.

Fig. 5. AlphaFold structural prediction reveals putative nucleic acid binding domains in SFTSV NSs protein.
Predicted three-dimensional structure of SFTSV NSs protein (NCBI Protein: AJD86041).
(**A)** Surface representation coloured by pLDDT confidence scores: very high confidence (dark blue, 90-100), confident (light blue, 70-89), low confidence (yellow, 50-69), very low confidence (orange, 0-49).
(B) Electrostatic surface potential showing positive (blue) and negative (red) charges.
(C) RNA-binding site prediction using RBDetect analysis. Plot shows probability of RNA binding (y-axis) versus amino acid position (x-axis). Regions between dotted lines indicate high predicted RNA-binding propensity.
(D) Predicted RNA-binding residues mapped onto the protein surface: RBDetect predictions (dark green) and BindUP predictions (light green).

Fig. 6. SFTSV NSs binds viral single-stranded RNA in infected BME/CTVM6 cells.
(A) Immunoprecipitation of V5-tagged NSs proteins to assess NSs-vsiRNA interactions during SFTSV infection. BME/CTVM6 cells infected with SFTSV expressing either deletion mutant NSs-p19V5 (delNSs-p19V5) or wild-type V5-tagged NSs (wt-NSsV5) were harvested at 2 dpi and subjected to immunoprecipitation using anti-V5 antibody. Whole cell lysates (WCL; input) and immunoprecipitates (IP) were analysed by Western blot using anti-tubulin (loading control) and anti-V5 antibodies. RNA was subsequently extracted from immunoprecipitates for small RNA sequencing analysis. Molecular weights (kDa) are indicated. Data represent n=3 biological replicates (Replicate 1-3).
(B) Histogram of all small RNA reads (18-30 nt) in immunoprecipitated samples, p19V5 i.p. (left panel) or NSsV5 i.p. (right panel) representative of n=3 biological replicates.
(C) Small RNA reads from (B) mapped to SFTSV antigenomic (positive values) and genomic (negative values) strand RNAs from p19V5 i.p. (left panel) and NSsV5 i.p. (right panel) samples at 2 dpi. Read counts are coloured by the identity of the 5′ nucleotide and grouped by read length. Data are shown as the mean percentage of total mapped reads (y-axis); representative of n=3 biological replicates.
(D) Distribution of small RNA reads (18-30 nt) mapping to SFTSV genome segments from p19V5 i.p. (left panel) and NSsV5 i.p. (right panel) samples at 2 dpi Data represent n=3 biological replicates.
(E) Mapping of 22-nt SFTSV-derived vsiRNAs across the S (left panel), M (middle panel), and L (right panel) genome segments in p19V5 i.p. samples (reads per million). Data show mapping to the SFTSV antigenomic (blue) or genomic (pink) strands; numbers indicate nucleotide positions. Representative data from n=3 biological replicates.
(F) Mapping of 22-nt SFTSV-derived vsiRNAs across genome segments in NSsV5 i.p. samples, as described in (C). Representative data from n=3 biological replicates.
(G) Histogram showing the percentage of 22-nt small RNA reads with 20-nt complementary overlap mapping to SFTSV genome or *R. microplus* genome (GCA_002176555.1) in whole cell lysate (WCL) and NSsV5 i.p. samples. Data represent n=3 biological replicates. Statistical analysis was performed using Brown-Forsythe and Welch's ANOVA with Dunnett's T3 multiple comparison test to compare percentage of RNA reads in duplexes between samples. Asterisks indicate significance: * $p \leq 0.05$, ** $p \leq 0.01$; ns = not significant.
(H-J) AlphaFold3-predicted structure of SFTSV non-structural protein NSs, shown as ribbon and surface representation (grey) bound to single-stranded viral small interfering RNA (vsiRNA, blue) generated during SFTSV infection of BME/CTVM6 tick cells (Fig. 6F) derived from the viral **(H)** S, **(I)** M and **(J)** L segments. Critical amino acids involved in RNA/protein binding to distances <4 Å are highlighted (brown). Green regions highlight key RNA-binding domains identified by RBDetect (Fig. 5C,D).

FIGURE LEGENDS FOR SUPPLEMENTARY INFORMATION

Supplementary Fig. 1. Beta-elimination on uninfected tick and mosquito cell cultures.
Histogram of all small RNA reads (18-30 nt) from uninfected BME/CTVM6 or AF525 (Ago2 knock out) cells after 3 days in culture. RNA was extracted from cell cultures and samples were either **(A)** untreated or **(B)** beta-eliminated. Read counts are coloured by the identity of the 5′ nucleotide and grouped by read length. Data are shown as mean reads as a percentage of the total small RNA sequencing library (y-axis); representative of n=3 biologically independent samples.

Supplementary Fig. 2. Beta-elimination in Semliki Forest virus-infected mosquito cell cultures.
An *Aedes aegypti* Ago2 knock out mosquito cell line (AF525) was infected with SFV (MOI: 10). At 24 h p.i., total cell RNA was extracted and either left untreated (top) or subjected to beta-elimination (bottom). Histograms of small RNA reads (18-30 nt) from **(A)** untreated or **(B)** beta-eliminated samples, mapped to the SFV genomic (negative values) and antigenomic (positive values) strand RNAs in infected cells. Read counts are coloured by the identity of the 5′ nucleotide and grouped by read length. Data are shown as the mean percentage of total mapped reads (y-axis); representative of n=3 biologically independent samples. **(C, D)** SFV-derived 21 nt vsiRNAs in **(C)** untreated or **(D)** beta-eliminated samples. Coverage across the viral genome for genomic (orange) and antigenomic (yellow) sense RNAs is shown (y-axis: vsiRNA reads per million) representatives of n=3 biologically independent samples.

Supplementary Fig. 3. Distribution of overlapping 21 nt vsiRNA pairs in SFV-infected AF525 cells.
Reanalysis of data from Supplementary Fig. 2. **(A)** Distribution of overlapping 21 nt vsiRNA pairs by nucleotide overlap length across the SFV genome (SFV4, GenBank ID: KP699763), presented as normalised per million mapped SFV reads. **(B)** Heat maps showing overlap probability z-scores for vsiRNAs of different lengths (x-axis) and overlap positions (y-axis) from three independent samples. Black boxes highlight the characteristic 2 nt overlap signature of Dicer-2 processing. Colour scale represents z-score values from -6 (teal) to +6 (purple).

Supplementary Fig. 4. Characterisation of delNSs-p19V5 SFTSV in Vero E6 cells.
(A) Western blot analysis of viral protein expression in infected Vero E6 cells (6 dpi; MOI: 1). Blots were probed with antibodies against tubulin (loading control), SFTSV NSs, SFTSV N, or V5 tag. Lane labels: wt, wild-type SFTSV; G, delNSs-eGFP; p19, delNSs-p19V5. Viral replication kinetics in BME/CTVM6 cells infected with wild-type SFTSV (teal), delNSs-p19V5 (red), or delNSs-eGFP (black) viruses. Virus titres were determined by focus-forming assay at indicated time points. Data show one representative experiment from n=3 independent experiments.
(B) Viral replication kinetics in Vero E6 cells infected with wild-type SFTSV (teal), delNSs-p19V5 (red), or delNSs-eGFP (black) viruses. Virus titres were determined by focus-forming assay at indicated time points. Data show one representative experiment from n=3 independent experiments.

Supplementary Fig. 5. AlphaFold structural prediction confidence metrics for SFTSV NSs protein.
(A) Multiple sequence alignment heatmap for SFTSV NSs protein (NCBI Protein: AJD86041) and homologs. Colour scale represents sequence identity from low (red, 0.0) to high (blue, 1.0) conservation. Black line shows position-specific conservation scores. **(B)** Per-residue confidence (pLDDT) scores across AlphaFold model ranks. Blue shading highlights highest confidence region. **(C)** Inter-domain positioning confidence (pTM) scores across model ranks. Yellow shading indicates optimal predictions. **(D)** Predicted Aligned Error (PAE) matrices for top 10 ranked models showing residue-residue distance confidence. Colour scale represents predicted error (0-30 Ångströms), with blue indicating high confidence and red showing uncertainty. **(E)** Rank 1 structure coloured by pLLDT confidence: very high (dark blue: 90-100), confident (light blue: 70-89), low (yellow: 50-69), very low (orange: 0-49). **(F)** Rank 1 structure with rainbow colouring from N-terminus (blue) to C-terminus (red).

Supplementary Fig. 6. Total mapped reads and strand-specific reads for each replicate of Fig. 6B,C.
Histogram of all small RNA reads (18-30 nt) in samples immunoprecipitated with anti-V5 antibodies at 2 dpi from **(A)** p19V5 or **(B)** NSsV5 SFTSV-infected BME/CTVM6 cells (Replicates 1-3). **(C,D)** Small RNA reads from individual replicates mapped to SFTSV antigenomic (positive values) and genomic (negative values) strand RNAs from **(C)** p19V5 and **(D)** NSsV5 immunoprecipitation samples. Read counts are coloured by 5′ nucleotide identity and grouped by read length. Data are shown as percentage of total mapped reads for each individual biological replicate (n=3).

Supplementary Fig. 7. Mapping of 22-nt SFTSV-derived vsiRNAs for each replicate of Fig. 6E.
Mapping of 22-nt SFTSV-derived vsiRNAs across the S (left panel), M (middle panel), and L (right panel) genome segments in p19V5 immunoprecipitation samples (replicates 1-3; reads per million). Data show mapping to the SFTSV antigenomic (blue) or genomic (pink) strands with nucleotide positions indicated. Individual biological replicates (n=3) are shown as mapped read counts at each nucleotide position.

Supplementary Fig. 8. Mapping of 22-nt SFTSV-derived vsiRNAs for each replicate of Fig. 6F.
Mapping of 22-nt SFTSV-derived vsiRNAs across the S (left panel), M (middle panel), and L (right panel) genome segments in NSsV5 immunoprecipitation samples (replicates 1-3; reads per million). Data show mapping to the

SFTSV antigenomic (blue) or genomic (pink) strands with nucleotide positions indicated. Mapped read counts at each nucleotide position are shown for individual biological replicates (n=3).

Supplementary Fig. 9. Secondary structure of the SFTSV antigenomic S RNA (HB29 strain) showing mapping sites of vsiRNAs immunoprecipitated with NSs from infected cells.

Secondary structure prediction of a 76-nucleotide sequence (positions 1191-1266) from the antigenomic sense SFTSV S segment RNA (HB29 strain, GenBank: KP202165). Structure was predicted using minimum free energy folding calculations with Turner energy parameters at 37°C via the Forna web server powered by the ViennaRNA package. Orange circles indicate 22-nucleotide siRNAs identified through NSs immunoprecipitation and small RNA sequencing. The distribution of NSs-bound siRNAs across stem-loop and single-stranded regions demonstrates the RNA-binding specificity of NSs and supports its function as a viral suppressor of RNA silencing that sequesters host siRNAs.

Supplementary Fig. 10. Additional detected RNA duplexes of differing sizes in immunoprecipitated samples from Fig. 6.

Histograms showing the percentage of small RNA reads in duplexes with complementary overlaps: **(A)** 21-nt reads with 19-nt overlap, **(B)** 23-nt reads with 21-nt overlap, **(C)** 24-nt reads with 22-nt overlap, and **(D)** 28-nt reads with 10-nt overlap. Reads were mapped to SFTSV genome or *R. microplus* genome (GCA_002176555.1) in whole cell lysate (WCL) and NSsV5 immunoprecipitation (i.p.) samples. Data represent n=3 biological replicates. Statistical significance was determined using Brown-Forsythe and Welch's ANOVA with Dunnett's T3 multiple comparison test. Asterisks indicate significance: * $p \leq 0.05$, ** $p \leq 0.01$; ns = not significant.

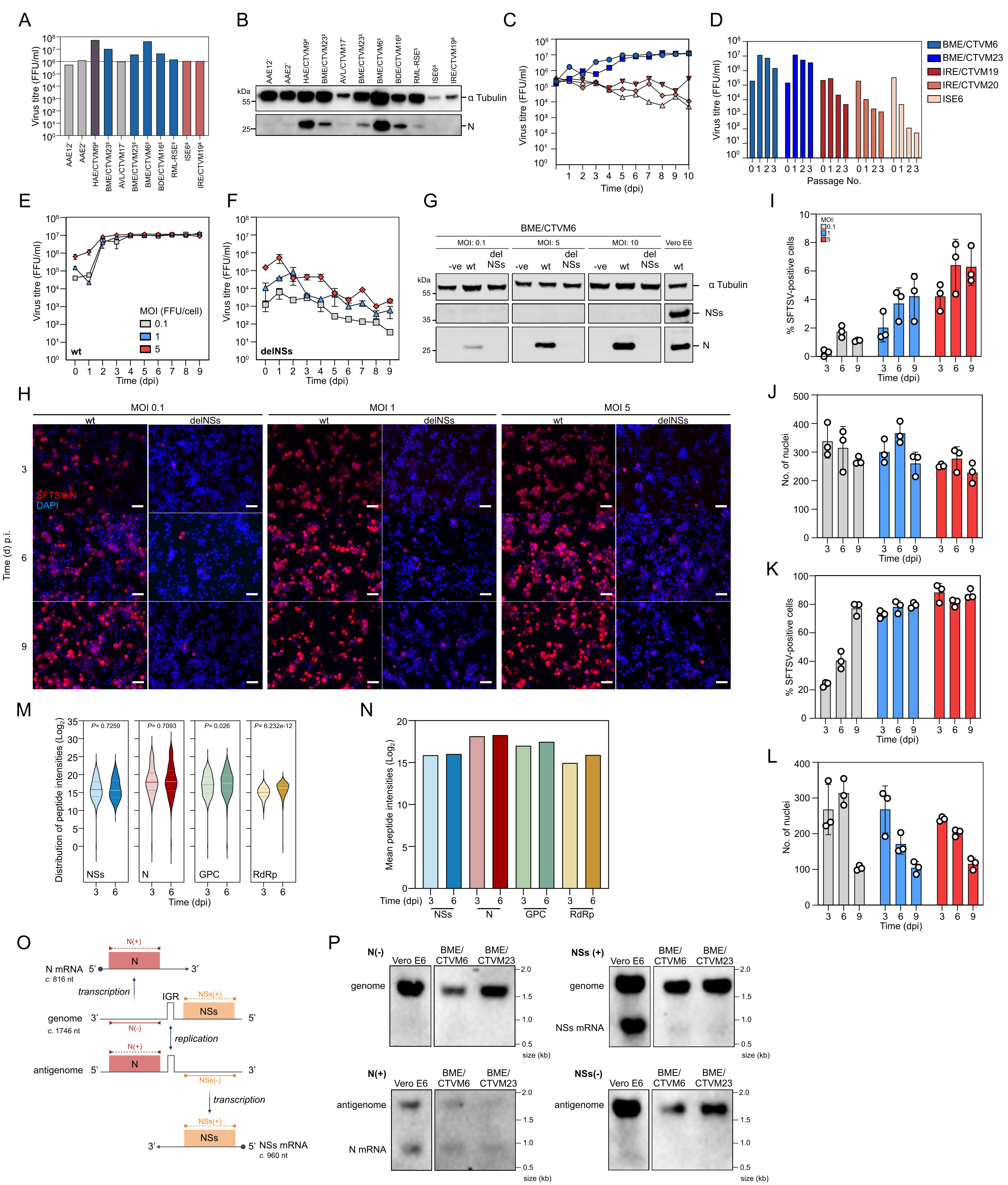
A
Virus titre (FFU/ml)
AAE12*
AAE2*
HAE/CTVM9#
BME/CTVM23$
AVL/CTVM17*
BME/CTVM23$
BME/CTVM6$
BDE/CTVM16$
RML-RSE$
ISE6&
IRE/CTVM19&
B
kDa
55
25
α Tubulin
N
C
Virus titre (FFU/ml)
Time (dpi)
D
Virus titre (FFU/ml)
Passage No.
BME/CTVM6
BME/CTVM23
IRE/CTVM19
IRE/CTVM20
ISE6
E
Virus titre (FFU/ml)
MOI (FFU/cell)
0.1
1
5
wt
Time (dpi)
F
Virus titre (FFU/ml)
delNSs
Time (dpi)
G
BME/CTVM6
MOI: 0.1
MOI: 5
MOI: 10
Vero E6
-ve
wt
del NSs
kDa
55
35
25
α Tubulin
NSs
N
I
% SFTSV-positive cells
MOI:
0.1
1
5
Time (dpi)
H
MOI 0.1
MOI 1
MOI 5
wt
delNSs
Time (d) p.i.
SFTSV-N
DAPI
J
No. of nuclei
Time (dpi)
K
% SFTSV-positive cells
Time (dpi)
L
No. of nuclei
Time (dpi)
M
Distribution of peptide intensities (Log2)
P= 0.7259
P= 0.7093
P= 0.026
P= 6.232e-12
NSs
N
GPC
RdRp
Time (dpi)
N
Mean peptide intensities (Log2)
Time (dpi)
NSs
N
GPC
RdRp
O
N(+)
N
N mRNA
c. 816 nt
5'
3'
transcription
IGR
NSs(+)
NSs
genome
c. 1746 nt
N(-)
replication
antigenome
NSs(-)
transcription
NSs mRNA
c. 960 nt
P
N(-)
Vero E6
BME/ CTVM6
BME/ CTVM23
genome
NSs (+)
NSs mRNA
N(+)
antigenome
N mRNA
NSs(-)
2.0
1.5
1.0
0.5
size (kb)

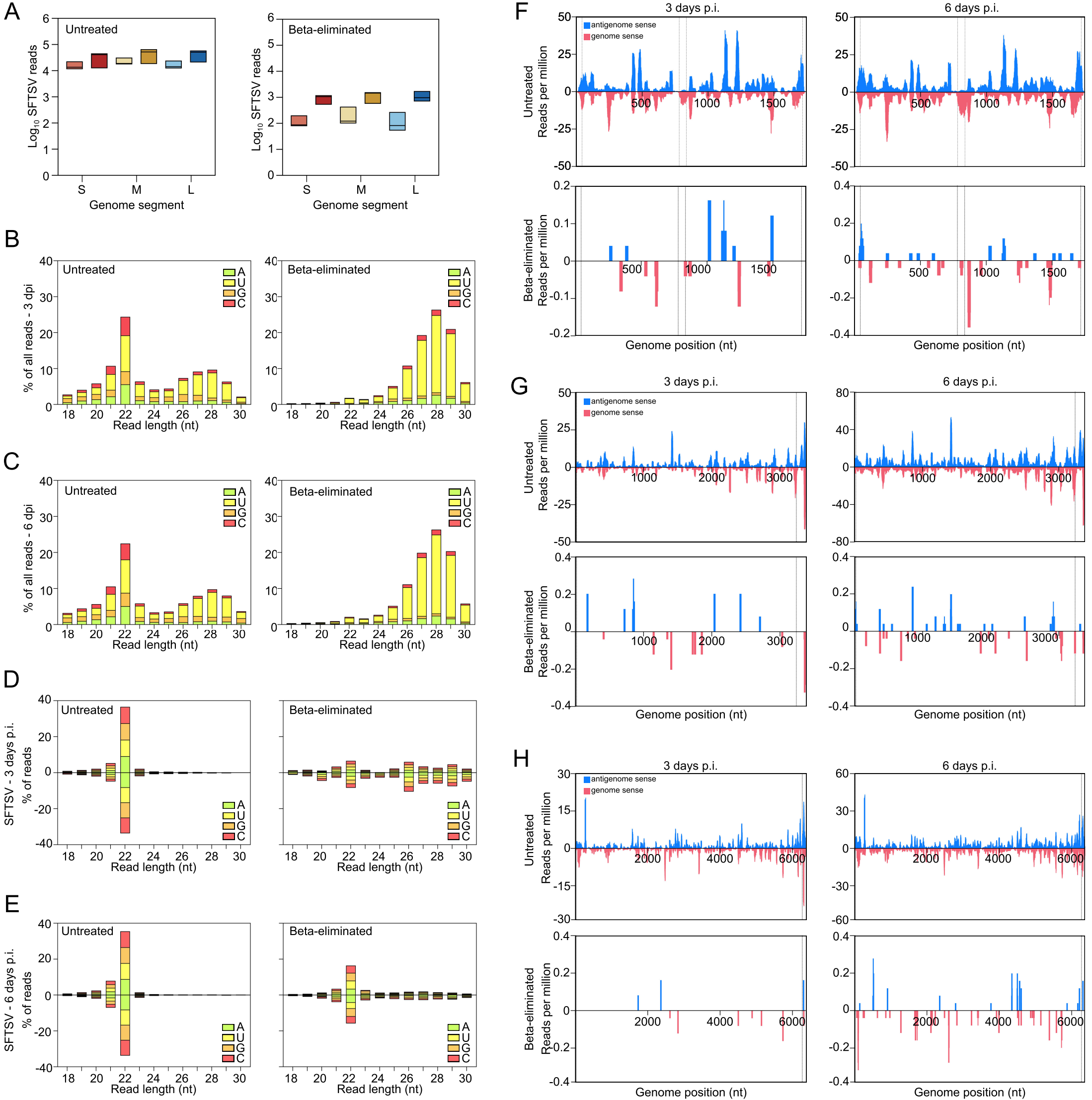
A
Untreated
Beta-eliminated
Log10 SFTSV reads
S
M
L
Genome segment
B
% of all reads - 3 dpi
Read length (nt)
C
% of all reads - 6 dpi
D
SFTSV - 3 days p.i.
% of reads
E
SFTSV - 6 days p.i.
A
U
G
C
F
3 days p.i.
6 days p.i.
antigenome sense
genome sense
Untreated
Reads per million
Beta-eliminated
Genome position (nt)
G
H

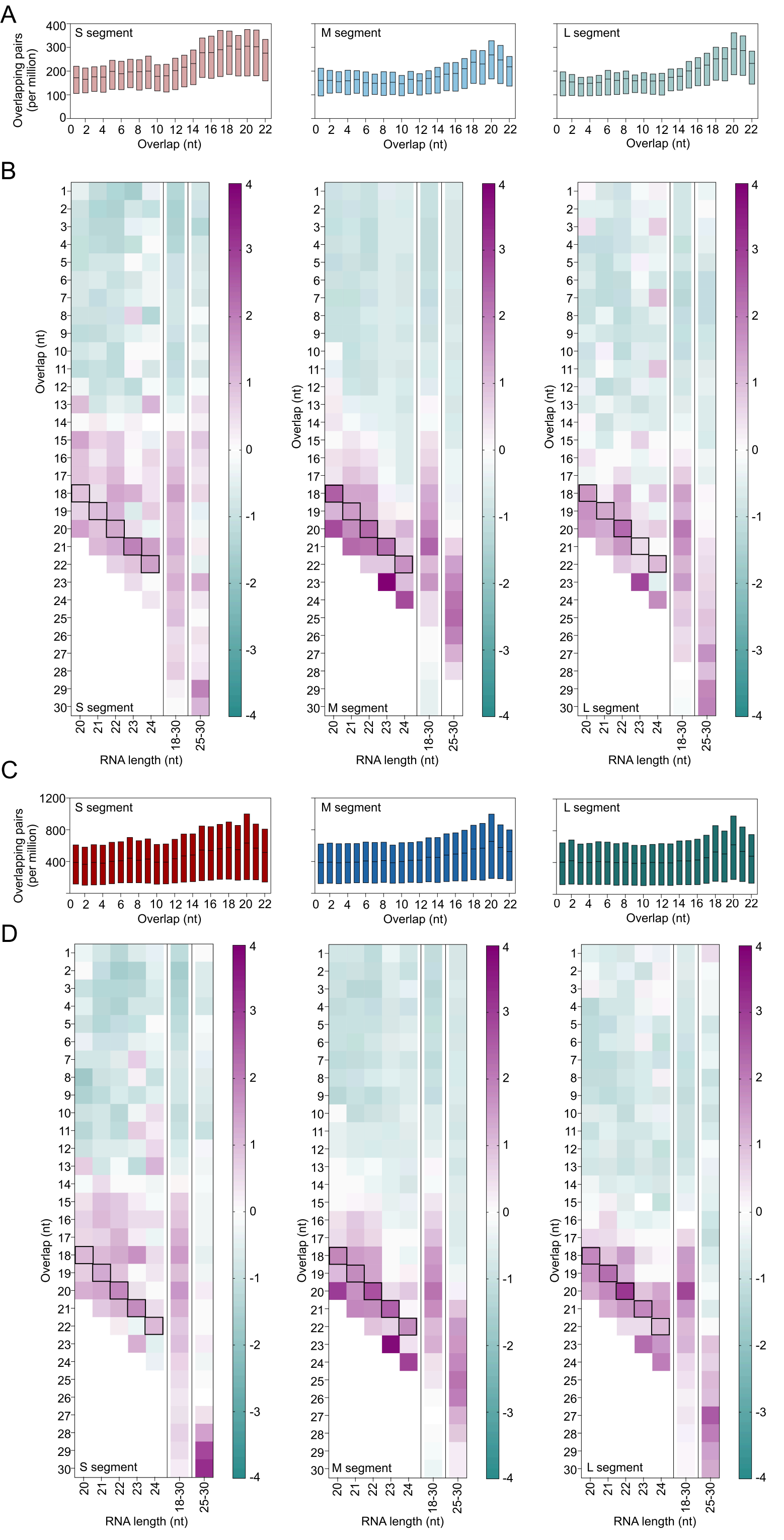
A
S segment
M segment
L segment
Overlapping pairs (per million)
Overlap (nt)
B
Overlap (nt)
RNA length (nt)
C
D

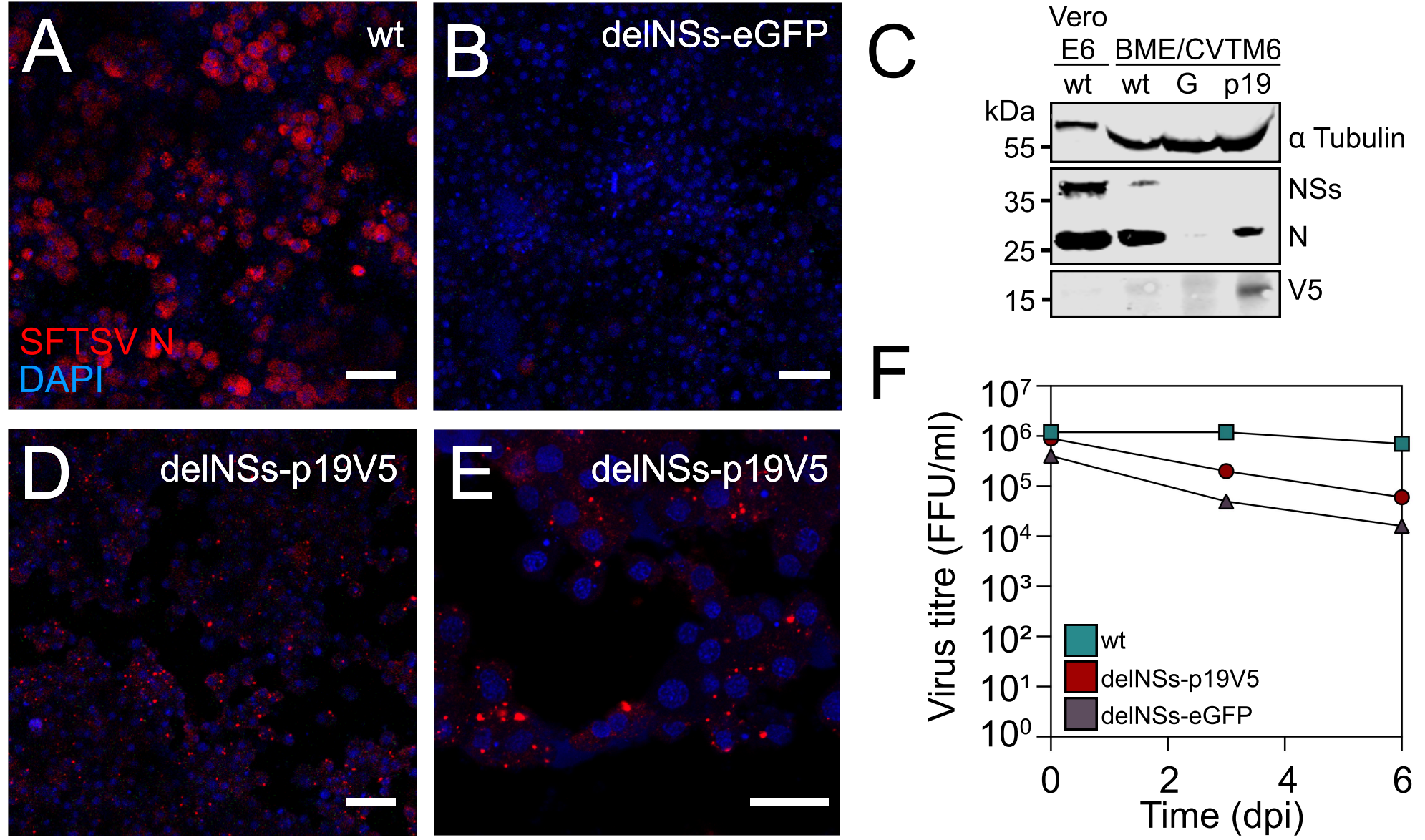
A
wt
SFTSV N
DAPI
B
delNSs-eGFP
C
Vero E6
BME/CVTM6
wt
wt
G
p19
kDa
55
35
25
15
α Tubulin
NSs
N
V5
D
delNSs-p19V5
E
delNSs-p19V5
F
Virus titre (FFU/ml)
10^7
10^6
10^5
10^4
10^3
10^2
10^1
10^0
wt
delNSs-p19V5
delNSs-eGFP
0
2
4
6
Time (dpi)

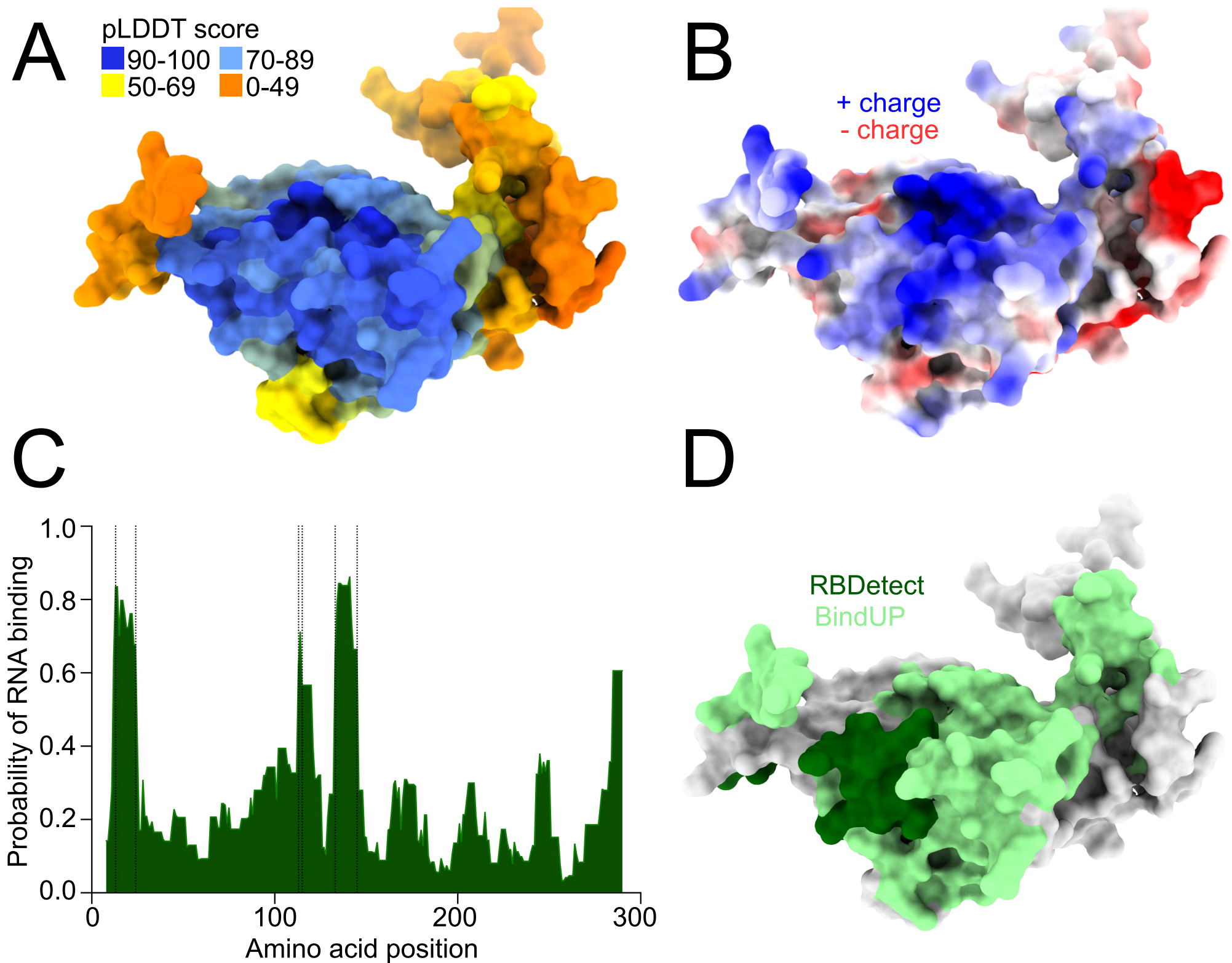
A
pLDDT score
90-100
70-89
50-69
0-49
B
+ charge
- charge
C
Probability of RNA binding
1.0
0.8
0.6
0.4
0.2
0.0
0
100
200
300
Amino acid position
D
RBDetect
BindUP

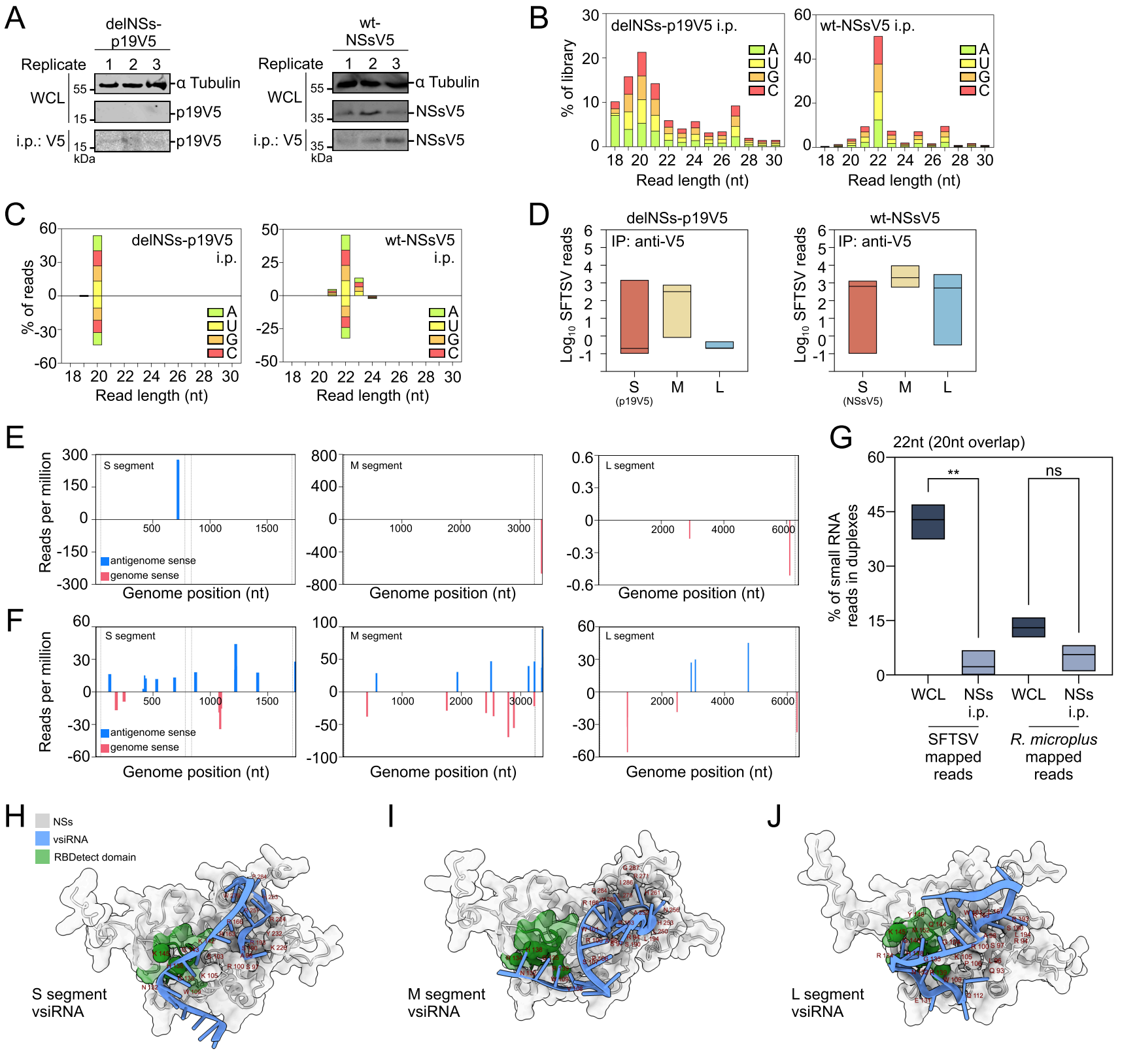
A
delNSs-p19V5
wt-NSsV5
Replicate 1 2 3
WCL
i.p.: V5
α Tubulin
p19V5
NSsV5
kDa
B
delNSs-p19V5 i.p.
wt-NSsV5 i.p.
% of library
Read length (nt)
A
U
G
C
C
delNSs-p19V5 i.p.
wt-NSsV5 i.p.
% of reads
D
delNSs-p19V5
wt-NSsV5
IP: anti-V5
Log10 SFTSV reads
S (p19V5)
M
L
S (NSsV5)
E
S segment
M segment
L segment
Reads per million
Genome position (nt)
antigenome sense
genome sense
F
G
22nt (20nt overlap)
% of small RNA reads in duplexes
**
ns
WCL
NSs i.p.
SFTSV mapped reads
R. microplus mapped reads
H
NSs
vsiRNA
RBDetect domain
S segment vsiRNA
I
M segment vsiRNA
J
L segment vsiRNA